NASA/TM—2018-219898/REV1

Dual Rotating Rake Measurements to Separate Incident and Reflected Spinning Duct Modes: Validation Using Experimental and Numerical Data

Milo D. Dahl
Glenn Research Center, Cleveland, Ohio

Duane R. Hixon
University of Toledo, Toledo, Ohio

Daniel L. Sutliff
Glenn Research Center, Cleveland, Ohio

This Revised Copy, numbered as NASA/TM—2018-219898/REV1, August 2018, supersedes the previous version, NASA/TM—2018-219898, May 2018, in its entirety.

August 2018

NASA STI Program . . . in Profile

Since its founding, NASA has been dedicated to the advancement of aeronautics and space science. The NASA Scientific and Technical Information (STI) Program plays a key part in helping NASA maintain this important role.

The NASA STI Program operates under the auspices of the Agency Chief Information Officer. It collects, organizes, provides for archiving, and disseminates NASA's STI. The NASA STI Program provides access to the NASA Technical Report Server—Registered (NTRS Reg) and NASA Technical Report Server—Public (NTRS) thus providing one of the largest collections of aeronautical and space science STI in the world. Results are published in both non-NASA channels and by NASA in the NASA STI Report Series, which includes the following report types:

- TECHNICAL PUBLICATION. Reports of completed research or a major significant phase of research that present the results of NASA programs and include extensive data or theoretical analysis. Includes compilations of significant scientific and technical data and information deemed to be of continuing reference value. NASA counter-part of peer-reviewed formal professional papers, but has less stringent limitations on manuscript length and extent of graphic presentations.

- TECHNICAL MEMORANDUM. Scientific and technical findings that are preliminary or of specialized interest, e.g., "quick-release" reports, working papers, and bibliographies that contain minimal annotation. Does not contain extensive analysis.

- CONTRACTOR REPORT. Scientific and technical findings by NASA-sponsored contractors and grantees.

- CONFERENCE PUBLICATION. Collected papers from scientific and technical conferences, symposia, seminars, or other meetings sponsored or co-sponsored by NASA.

- SPECIAL PUBLICATION. Scientific, technical, or historical information from NASA programs, projects, and missions, often concerned with subjects having substantial public interest.

- TECHNICAL TRANSLATION. English-language translations of foreign scientific and technical material pertinent to NASA's mission.

For more information about the NASA STI program, see the following:

- Access the NASA STI program home page at http://www.sti.nasa.gov

- E-mail your question to help@sti.nasa.gov

- Fax your question to the NASA STI Information Desk at 757-864-6500

- Telephone the NASA STI Information Desk at 757-864-9658

- Write to:
  NASA STI Program
  Mail Stop 148
  NASA Langley Research Center
  Hampton, VA 23681-2199

NASA/TM—2018-219898/REV1

Dual Rotating Rake Measurements to Separate Incident and Reflected Spinning Duct Modes: Validation Using Experimental and Numerical Data

Milo D. Dahl
Glenn Research Center, Cleveland, Ohio

Duane R. Hixon
University of Toledo, Toledo, Ohio

Daniel L. Sutliff
Glenn Research Center, Cleveland, Ohio

This Revised Copy, numbered as NASA/TM—2018-219898/REV1, August 2018, supersedes the previous version, NASA/TM—2018-219898, May 2018, in its entirety.

National Aeronautics and
Space Administration

Glenn Research Center
Cleveland, Ohio 44135

August 2018

Acknowledgments

The NASA Fixed Wing Project of the Fundamental Aeronautics Program and the NASA Advanced Air Transport Technology Project of the Advanced Air Vehicles Program supported this work.

Revised Copy

This Revised Copy, numbered as NASA/TM—2018-219898/REV1, August 2018, supersedes the previous version, NASA/TM—2018-219898, May 2018, in its entirety.

An incorrect draft version of NASA/TM—2018-219898 was published in May 2018. Modifications to this Revised Copy address errors, omissions, and inconsistencies to the title, text, figures, tables, and equations.

This work was sponsored by the Advanced Air Vehicle Program at the NASA Glenn Research Center.

Level of Review: This material has been technically reviewed by technical management.

Available from

NASA STI Program
Mail Stop 148
NASA Langley Research Center
Hampton, VA 23681-2199

National Technical Information Service
5285 Port Royal Road
Springfield, VA 22161
703-605-6000

This report is available in electronic form at http://www.sti.nasa.gov/ and http://ntrs.nasa.gov/

Dual Rotating Rake Measurements to Separate Incident and Reflected Spinning Duct Modes: Validation Using Experimental and Numerical Data

Milo D. Dahl
National Aeronautics and Space Administration
Glenn Research Center
Cleveland, Ohio 44135

Duane R. Hixon
University of Toledo
Toledo, Ohio 43606

Daniel L. Sutliff
National Aeronautics and Space Administration
Glenn Research Center
Cleveland, Ohio 44135

A rotating rake mode measurement system was designed to measure acoustic duct modes generated by a fan stage. After analysis of the measured data, the mode coefficient amplitudes and phases were quantified. Early studies using this system found that mode power levels computed from rotating rake measured data would agree with the far-field power levels. However, this agreement required that the sound from the noise sources within the duct propagated outward from the duct exit without reflection and previous studies suggested conditions could exist where significant reflections could occur. This paper shows that mounting a second rake to the rotating system, with an offset in both the axial and the azimuthal directions, measures the data necessary to determine the modes propagating in both directions within a duct. The rotating rake data analysis technique was extended to include the data measured by the second rake. The analysis resulted in a set of circumferential mode coefficients at each of the two rake microphone locations. Radial basis functions were then least-squares fit to this data to obtain the radial mode coefficients for the modes propagating in both directions within the duct while accounting for the presence of evanescent modes. The validation of the dual-rotating-rake measurements was conducted using data from a combination of experiments and numerical calculations to compute reflection coefficients and other mode coefficient ratios. Compared to results from analytical and numerical computations, the results from dual-rotating-rake measured data followed the expected trends when frequency, mode number, and duct termination geometry were changed.

I. Introduction

A common source of sound generated within a ducted system is a rotating fan near a fixed stator. The wakes of the fan interact with the stator vanes producing an unsteady pressure field in response. In a turbofan

engine for example, the sound is caused by this rotor-stator interaction plus other interactions. Inside the duct, the source generated sound couples to spinning duct modes that propagate through and radiate outward from the duct to the far field. A rotating microphone system is a method to measure and identify these spinning duct modes. Placed on a rake mounted in a fan duct and rotating at a fraction of the fan shaft speed, the microphones measure the interaction modes of the ducted fan and stator system. By continuously rotating the microphone system in a manner locked to the fan shaft but at a slower speed, a Doppler shift is imparted to the measurement of the duct modes making individual co-rotating and counter-rotating modes easily identifiable.[1] The success of the technique depends on the data analysis or post-processing of the measured signals from the microphones. The coefficients computed from the Fourier transform of the microphone signals represent the complex circumferential mode coefficients (each with amplitude and phase) of the spinning modes of the measured acoustic pressure field in the duct. These circumferential modes are further decomposed into a finite set of radial basis functions representing the radial modal structure of the acoustic field. The mode coefficients of the radial basis functions are determined by a least-squares fit of the functions to the complex circumferential mode coefficients at the radial microphone locations. Hall et al.[2] developed the original data processing technique for a rotating-rake, microphone measurement system where the radial basis functions were the closed-form solutions (i.e., the Bessel functions) to the equation for sound propagating in a hard-wall, circular duct with no mean flow. This type of analysis was subsequently extended by Sutliff[3–5] to include the effects of a constant mean flow in a soft-wall duct. The closed-form solutions were still applied and the duct cross-section could be circular or annular. For the general case where a boundary layer exists at the wall of the duct, the data analysis using closed-form solutions may not be sufficiently accurate. Dahl & Sutliff[6] presented a numerical technique for computing the radial basis functions that are necessary for the proper analysis of the data from rotating rake mode measurements in a duct with non-uniform flow and improved the accuracy of the obtained mode coefficients.[7]

In addition to the effect of the flow profile on the shape of the radial basis functions, Dahl & Sutliff[6] discussed the assumption that the mode coefficient results were based on modes propagating in only one direction. Heidelberg & Hall[8] recognized that this was an issue during early development of the rotating rake measurement system. The presence of reflected modes would confuse the interpretation of the measured data. But, since the far-field sound computed from in-duct measured mode data had good agreement with measured far-field radiated sound levels, they assumed that most of the acoustic power was traveling away from the fan and stator sound sources and hence the acoustic modes behaved the same way. Nonetheless, to account for the presence of reflected mode contamination in rotating rake measured data, Cicon & Sofrin[9] developed a scheme using a finite element radiation code to produce calibration values that related the measured total sound to the sound propagating away from the source and toward the inlet or exit of the duct. They showed that depending on the location of the rotating rake measurement plane within the duct, the far-field sound levels based on that data varied over a range of 12 dB. Using the calibration scheme, this range was reduced to a ± 0.5 dB band. Thus, the reflected mode effects could be removed from already measured data. Meyer[10] further studied the effects of reflections in a fan inlet duct using a numerical code to predict the sound source coupled to a code that computes the radiated sound from within the duct. The most significant effects were found in the frequency range nearest to where the mode cuts on. This effect was later confirmed by Nallasamy et al.[11] where it was shown that mode reflections increase as cutoff is approached. The resulting changes in far-field sound levels were reported as high as 3 dB.

A simple illustration of the effects on the results of neglecting reflected modes when analyzing rotating-rake measurements is shown in Fig. 1. One mode is known to propagate in a duct and, because of the duct termination, this mode reflects and generates the same type of mode propagating in the opposite direction.

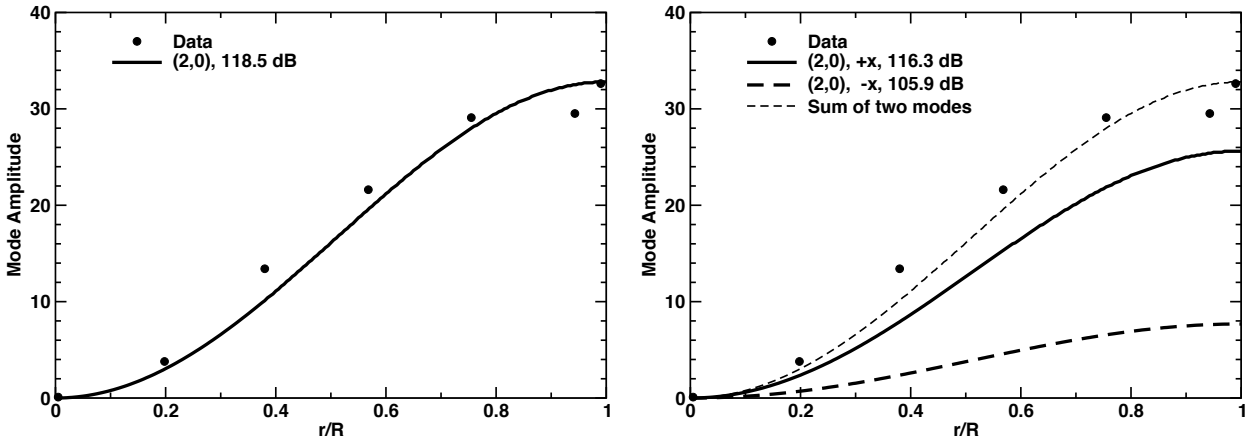

(a) (b)

Fig. 1. Example of mode shapes and propagating mode power levels from single-rake and dual-rake analyses of measured rake data in a duct with a mode propagating in both directions. (a) Mode from single-rake analysis. (b) $+x$ and $-x$ modes from dual-rake analysis.

One rotating rake with seven radially distributed microphones measured the acoustic field within the duct at one axial location. The results from the single-rake data analysis for the best-fit, single mode shape across the duct radius where the mode is assumed to be propagating in one direction, the $+x$ direction, is shown in Fig. 1(a) compared to amplitudes of the measured data. The radial variable r is normalized by the duct radius R. The mode shape fits the data well. The mode power level is shown to be 118.5 dB. The measurements were repeated with two axially-offset rakes. Figure 1(b) shows the best-fit, mode shape results from the dual-rake system analysis where a $+x$-direction propagating mode and a $-x$-direction propagating mode are obtained. Note that the amplitude of the sum of the two opposite direction propagating modes fits the data well at the same axial location as shown in Fig. 1(a) for the single-rake results. The mode power levels are shown to be 116.3 dB for the $+x$-direction mode and 105.9 dB for the $-x$-direction mode. Hence, the acoustic energy is largely propagating in the $+x$ direction. As we noted, it has been common practice to estimate radiated mode power levels using data from a single-rake measurement. In this case, the single-rake mode power level is overestimating the true radiated mode power level by about 2 dB.

This paper uses the data generated from experiment and from numerical calculation to validate the extension of the single-rotating-rake measurement method and data analysis as previously described[1,2,5,6] to include the addition of a second rake, offset axially and co-rotating with the original single rake, enabling the separation of the modes propagating in both directions in a duct. This will provide a better tool for diagnosing the sound structure in a fan duct especially as large, modern fans are designed with shorter inlet ducts. The length of the duct, whether long or short, affects the level of reflections in the duct, as alluded to in Heidelberg & Hall[8] and Meyer.[10] The duct length also determines the amount of acoustic treatment that can be placed in the duct which can affect the amount of reflection at the exit[12,13] and hence the amount of radiated sound.

In the next section, a description of the experimental facility is given followed by a brief presentation of the dual-rotating rake data analysis. A more extensive review of mode measurement data analysis for both a fixed array of microphones and a rotating array of microphones is presented in the appendices. Next, results are given for a single propagating mode incident upon the end of the duct with two different geometric configurations, comparing mode amplitudes and mode powers between single- and dual-rake results. To determine the accuracy of the experimental results and to aid in the analysis of the experimental measurements with

multiple propagating modes, numerical calculations were performed to simulate the mode propagation in an open end duct. The numerical data generated from a computational aeroacoustics code[14] was post-processed using a fixed-array analysis technique.

The NASA Glenn Broadband Aeroacoustic Stator Simulation (BASS) code was used to perform the numerical computations. A description of the numerical code and some computational details are given. The data from the simulated acoustic field inside a circular duct was used to compute mode reflection and conversion coefficients for each of the following reference geometries:

1. The thin duct ends abruptly with no flange.

2. The duct exit has an infinite flange.

3. The duct exit transitions to a hyperboloidal shape extending to infinity.

For each of these geometries, the reflection and conversion coefficients can also be analytically computed. These coefficients depend on the physics of the acoustic modes interacting with the geometry of the duct exit and do not depend on the amplitude and phase of the source generated acoustic modes (linear assumption). Hence, they are used for comparing results determined from multiple experimentally measured and numerically generated data sets. The BASS calculated coefficients converged to the analytical results with grid refinement. With confidence in the computed solutions, the numerical code was used to simulate the experimental duct facility.

With artificial sources generating propagating acoustic modes in the experimental duct facility, dual-rotating-rake measurements were conducted with the following acoustic conditions:

1. One propagating mode in each direction with no other propagating modes.

2. Three propagating modes in each direction where each incident mode generates some portion of the 'reflected' modes due to reflection of the incident mode and conversion to other propagating modes.

The results of these measurements using reflection coefficients and other ratios of mode coefficients show that the expected trends are followed with changes in frequency, mode number, and duct termination geometry compared to results from analytical theory and numerical computations and that the error levels are similar to those found in reflection and conversion coefficient results obtained using other measurement techniques.

II. Experimental Measurements

Initial experiments to validate the dual-rotating rake mode measurement system and data analysis were conducted as part of a larger study to develop a database useful for validation of numerical simulations of duct mode propagation with various physical configurations.[13] After a description of the experimental facility and the data analysis, results from the measurement of a single propagating mode in the duct are presented. To validate these results and to aid in the analysis of multi-modal propagation results, numerical calculations were performed as described in the next section.

II.A. Facility

The NASA Advanced Noise Control Fan (ANCF)[15] experiment rig was a highly configurable, segmented duct, 1.22 m (4 feet) in diameter, with an incorporated fan that during experimental operation was located in the Aero-Acoustic Propulsion Laboratory (AAPL) at the NASA Glenn Research Center. The AAPL is a hemispherical, anechoic (above 125 Hz) test facility that provides a reflection-free environment for radiated

sound measurements. In order to provide a clean, cylindrical duct, for this experiment, the ANCF spool segments were stacked in a vertical orientation, with the fan assembly removed, providing a constant area cylindrical duct. The entire stack rested on the floor with approximately 15.2 cm (6 inches) of foam material placed in the bottom of the stack to minimize reflections from the floor. Testing in this experimental duct facility was conducted with two configurations. In one configuration, a flow lip was attached to the duct exit as shown schematically in Fig. 2. The lip was removed in the second configuration revealing a square-edged mounting flange at the exit and, for the experimental results, it is called the flange exit.

The Configurable Fan Artificial Noise System (CFANS)[13] was utilized to generate and control circumferential modes. The system consisted of four axially distributed rows, each containing 16 electromagnetic drivers distributed around the circumference. There were two spool segments, each having two rows of flush mounted drivers on the wall. A Labview^{TM}program was used to generate the signals sent to each driver independently, in the proper relationship, to generate the desired circumferential mode. The signals to each row could be adjusted globally to effect the radial distribution, if desired. For this experiment, only a single row was actuated, the row closest to the floor. The practical limits of the system were circumferential mode orders up to ± 7 and a maximum frequency of 1500 Hz. In addition, CFANS generated a signal that simulated the sampling frequency signal for the rotating rake data at the frequency of the measurement.

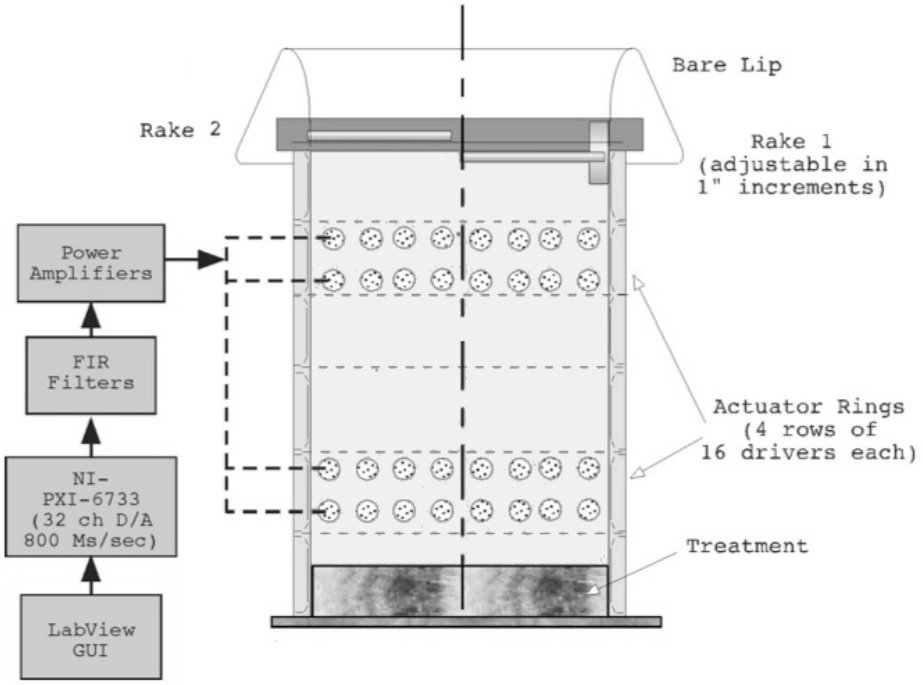

Fig. 2. Schematic diagram of the experimental duct facility, the Configurable Fan Artificial Noise System with signal generator and source actuator rings, and the installed rotating rakes.

The modes were measured by a rotating rake mode measurement system.[3] Typically, a single rake, extending from the outer-wall to the duct center-line, has been mounted to measure the modes. Since measurements at a single axial location were not able to account for reflections in the duct, an additional rake was mounted for the experiment on the same rotating ring as the original as shown in the left side of Fig. 3. This rake was adjustable in the axial direction over the range of 6.35 to 26.7 cm (2.5 to 10.5 inches), in fixed, 2.54 cm (1 inch) increments, and was mounted 180 degrees in the circumferential direction from the

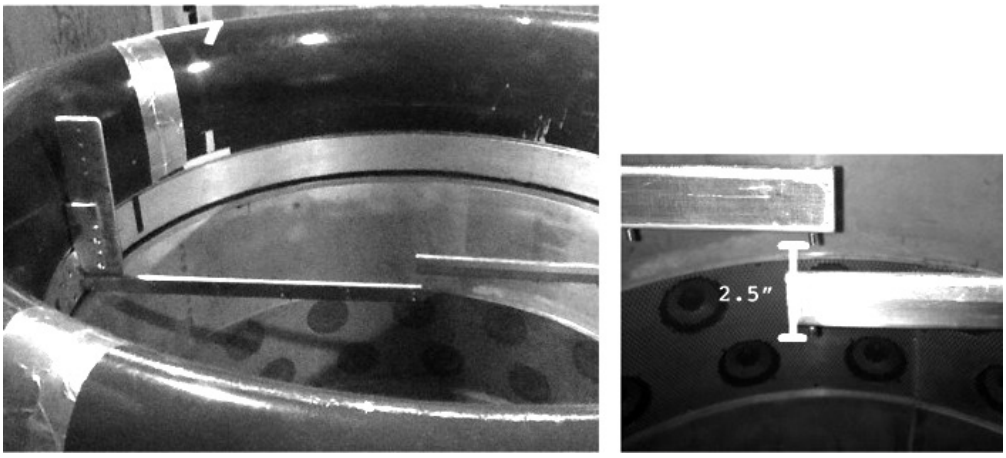

Fig. 3. Pictures of the two rotating rakes installed near the lip of the duct and a close-up of the rakes with a 6.35 cm (2.5 inch) separation distance.

original rake, which remains fixed in the axial direction. Seven microphones were mounted along each rake. Fig. 3 also shows a close up picture of the separation between the rakes.

II.B. Dual Rotating Rake Mode Measurement Data Analysis

The data collected from the rotating rakes were analyzed to obtain the mode coefficient for each of the measured modes. When data from one rotating rake were analyzed, the mode coefficients were a result of the superposition of modes propagating in both directions within the duct. The coefficients of the measured modes that propagate in both directions in the duct were obtained separately when data from two rotating rakes were analyzed. Once the mode coefficients were found, the acoustic power in each mode could be computed. For that to occur, two basic processes were followed: 1) determine the radial basis functions and 2) determine the mode coefficients by a least-squares fit using a system of equations representing modes propagating in one or both directions in the duct for data collected from one or two rotating rakes, respectively. The presence of decaying or evanescent modes were also accommodated in the fit for the case using the data from two rotating rakes.

II.B.1. Rotating Microphone Analysis

For a microphone in a rotating frame, the measured data were analyzed to obtain the circumferential mode coefficient at each radial measurement location. The acoustic pressure field in the duct, represented analytically as a combination of acoustic modes, was measured by a rotating microphone

$$p(x_1, \phi, r_1, t) = \mathrm{Re}\left\{ \sum_{s} \sum_{m=-M}^{M} C_m^s(x_1, r_1) e^{jm\phi} e^{-j2\pi(sB\Omega - m\Gamma)t} \right\} \tag{1}$$

where p is the real acoustic pressure that is shown to be a cyclical function of time t and the azimuthal direction since in a circular duct, the pressure must be repetitive in that direction. It is also shown to be a general summation of spatial modes $C_m^s(x, r)$ over frequencies and the circumferential mode index m where the index ranges over a finite number of modes denoted by the general value M. The source frequency $sB\Omega$ simulates the harmonic frequencies that are generated by a rotating fan with Ω, the shaft speed in revolutions per second, B, the number of blades, and, s, the harmonic number $s = 1, 2, \ldots$. The signal is sampled synchronously with the shaft speed and ensemble averaged over a period $T = I\Delta t$, I being the total

number of samples in the discrete time history. This reduces the uncorrelated broadband noise in favor of the tonal content of the signal.

A microphone generating a signal that is described by Eq. (1) is located at a fixed axial location x_1, a fixed radial location r_1, and at a rotating azimuthal location $2\pi\Gamma t + \phi$ where Γ is the rotational speed of the rake and ϕ is an azimuthal offset from some reference. Eq. (1) shows that the source blade passage frequency harmonic $sB\Omega$ has been Doppler shifted to $sB\Omega - m\Gamma$. Taking the discrete Fourier transform of the microphone signal,

$$\hat{P}(\ell) = \frac{1}{I}\sum_{i=0}^{I-1} p(i) e^{j2\pi\ell i/I} \qquad \ell = 0, 1, 2, \ldots, I-1, \tag{2}$$

we obtain for any spectral component of the signal:

$$\hat{P}_m^s(x_1, \phi, r_1, \ell) = \frac{1}{2} C_m^s(x_1, r_1) e^{jm\phi} \delta(n - \ell) + \frac{1}{2} C_m^{s*}(x_1, r_1) e^{-jm\phi} \delta(I - n - \ell) \tag{3}$$

where n must be an integer such that

$$n = n_r \left(\frac{sB\Omega}{\Gamma} - m \right) \tag{4}$$

and n_r is the number of rake revolutions in the time history T. Eq. (3) shows that the complex circumferential mode coefficients can be simply extracted using

$$C_m^s(x_1, r_1) = 2\hat{P}_m^s(x_1, \phi, r_1, \ell) e^{-jm\phi} \tag{5}$$

where $\ell = n$ for the desired harmonic number s and circumferential mode number m. Further details are given in Appendix A.

II.B.2. Radial Mode Content by Least-Squares Fit

The analysis of the rotating microphone signal has provided the complex circumferential mode coefficient $C_m^s(x_1, r_1)$ at the location of the microphone. Each circumferential mode coefficient is further decomposed into a weighted series of radial basis functions $E_{sm\mu}(r_\alpha; x_1)$ that for the N_1 microphone locations on the rake at x_1 and the N_2 microphone locations on the rake at x_2 may be represented as

$$\begin{aligned} C_m^s(x_1, r_\alpha) &= \sum_{\mu=0}^{N_{\max}^{\pm}-1} P_{sm\mu}^{\pm} E_{sm\mu}^{\pm}(r_\alpha; x_1) e^{jk_1^{\pm} x_1} \\ C_m^s(x_2, r'_{\alpha'}) e^{-jm\phi} &= \sum_{\mu=0}^{N_{\max}^{\pm}-1} P_{sm\mu}^{\pm} E_{sm\mu}^{\pm}(r'_{\alpha'}; x_2) e^{jk_2^{\pm} x_2} \\ & \qquad \alpha = 1, 2, \ldots, N_1 \qquad \alpha' = 1, 2, \ldots, N_2 \end{aligned} \tag{6}$$

where the $\pm$ notation indicates that there is a series of functions related to the $+x$-direction modes followed by an additional series related to the $-x$-direction modes. The axial wave numbers depend on the frequency through the harmonic number s and the mode numbers m and μ and the subscripts '1' and '2' apply for the solution for axial wave numbers at the rake locations x_1 and x_2. Also, r_α and $r'_{\alpha'}$ denote that radial locations of microphones on the two rakes may differ in location and number and ϕ is the azimuthal offset between the rake at x_1 and the rake at x_2. The form of Eq. (6) indicates that the measured data from both rakes were identically analyzed as if $\phi = 0$ in Eq. (5). For the least-squares fit, the rake at x_1 was chosen as the reference and the azimuthal offset ϕ was then added to the rake data from location x_2. Eq. (6) allows

for the presence of evanescent modes to be included in the fit for the mode coefficients. Fig. 2 shows the rakes located near the duct exit, a point of reflection, and away from the sources. In that configuration, evanescent modes may be generated by the reflections and decay past the rake location but none toward the exits since the source is far enough away. Thus, the total number of $+x$-direction modes, $N^+_{\max}$, included in the fit may differ from the total number of $-x$-direction modes, $N^-_{\max}$.

With the radial basis functions (described in Appendix B) previously computed at a frequency with harmonic number s and for the duct conditions at the rake axial locations x_1 and x_2, Eq. (6) is solved for the complex radial mode coefficients, $P^{\pm}_{sm\mu}$, using the least-squares method. The solution is to minimize the residual sum of squares

$$e = \|\mathbf{c} - \mathbf{BP}\|_2^2 \tag{7}$$

where $\mathbf{c}$ is a vector of length $n_p = N_1 + N_2$ comprised of the measured complex circumferential mode data, $\mathbf{B}$ is a matrix of size $n_p \times n_c$, $n_c = N^+_{\max} + N^-_{\max}$, containing complex coefficients derived from the radial basis functions, and $\mathbf{P}$ is the solution vector of length n_c for the complex radial mode coefficients at the current rake locations x_1 and x_2. The contents of each of these vectors and matrix are given in Appendix A including the adjustments made to the functions in $\mathbf{B}$ to properly account for the presence of evanescent modes and minimize the potential for $\mathbf{B}$ to be singular. By ensuring that the total number of measurement points n_p is greater than n_c, the problem is overdetermined and a solution to this linear problem is easily computed using the singular value decomposition method.[16]

II.C. Mode Amplitude and Power

The CFANS drivers were set to generate a circumferential mode with a frequency of 480 Hz. Under these conditions only one mode propagated in the experimental duct facility, the $(2, 0)$ mode. Initially, the flow lip was attached to the duct exit and a set of measurements were taken with one rake fixed and the movable rake at six different locations. The lip tends to minimize the reflection of sound within the duct and allows most of the sound generated to propagate out of the duct. The results of the data analysis for the amplitude of the complex mode coefficients from single-rake analysis using data from both the fixed rake (Rake 2 shown in Fig. 2) and the movable rake (Rake 1) are shown in Fig. 4a. The mode amplitude from the fixed rake data was computed for each measurement taken at the different movable rake locations. The average amplitude of the mode coefficient, 19.24 ± 0.09 Pa, for the fixed rake is plotted at its location $x/R = -0.083$ from the exit at $x = 0$, the open circle in Fig. 4. At each of the six movable rake locations, the data for the two rakes were collected simultaneously and used to perform the dual-rake analysis. The results show a fairly constant mode amplitude in both propagation directions with average amplitudes $|P^+_{20}| = 19.03 \pm 0.48$ Pa and $|P^-_{20}| = 2.89 \pm 0.20$ Pa (closed and open triangle symbols, respectively).

The other set of mode amplitude results, shown in Fig. 4b, were obtained using the same sound conditions and a second set of measurements but with the lip removed from the duct leaving the mounting flange at the duct exit. It was expected that the sound would more readily reflect back into the duct with this exit condition. The average fixed rake mode amplitude is 23.84 ± 0.15 Pa. The results show from the dual-rake analysis that, on average, the incident mode amplitude is $|P^+_{20}| = 19.88 \pm 0.47$ Pa, similar to the incident mode amplitude with the lip in place. However, the average reflected mode amplitude has doubled, $|P^-_{20}| = 5.81 \pm 0.29$ Pa.

The final comparison in Fig. 4 shows the standing wave amplitude computed from Eq. (C.2) versus the mode amplitude from the single-rake analysis of both the fixed rake and the movable rake data. The amplitudes determined from one-rake analysis are near the computed standing wave amplitudes with a maximum 5% error in Fig. 4a and a maximum 4% error in Fig. 4b. A fit of Eq. (C.2), using an unknown

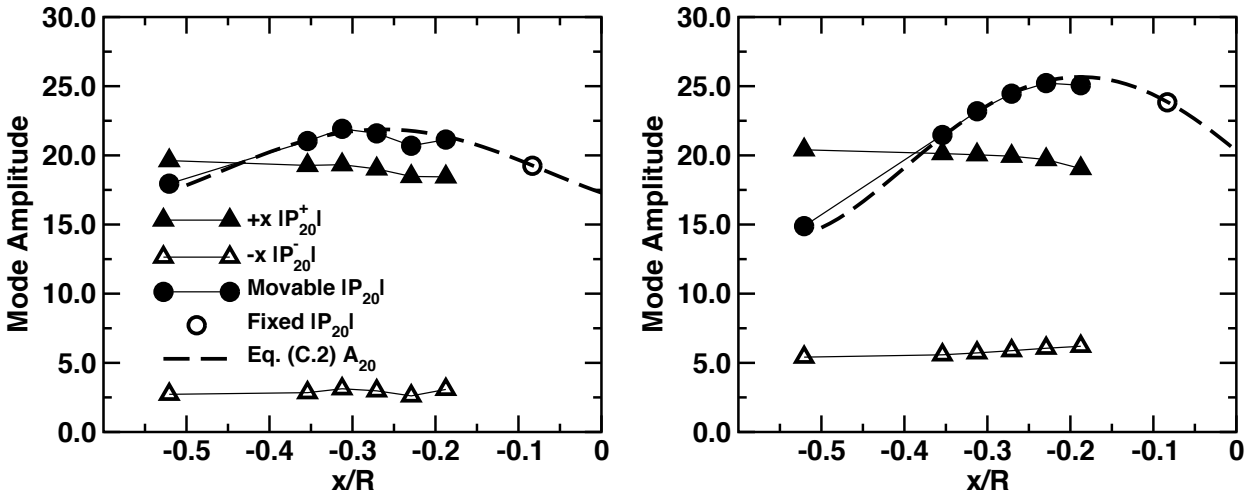

Fig. 4. Comparison of single-rake and dual-rake analyses for the mode amplitudes using in-duct measured data with different exit conditions. 480 Hz, mode $(2, 0)$. (a) Lip mounted at exit. (b) Flange exit.

distance added to x as the fit parameter, was performed. This resulted in a slight shift of the standing wave amplitude curves toward the source. For the lip exit condition, this distance was about 1.0 cm, and for the flange exit condition, 0.2 cm. These distances represent the combined uncertainties in knowing the axial locations of the point of reflection and the measurement microphones.

Table 1 compares the mode power results for the conditions and results just discussed for Fig. 4. The movable rake mode power levels indicate the variable range that would occur in the sound power levels when using only one rake, as discussed in Cicon & Sofrin.[9] In comparing the results between the two exit conditions, the dual-rake results show that the incident $+x$-direction mode power level remained about constant while the flange $-x$-direction mode power level increased by 6 dB over that of the lip exit condition. The final transmitted mode power remained constant between the two exit conditions. Previously, single-rake analysis results would be used to estimate the level of radiated sound. The Table 1 results show that the fixed rake mode power level is close (within 0.3 dB) to the transmitted mode power levels with the lip in place at the duct exit showing that in this case, the single-rake result gives a reasonable estimate of the transmitted sound power. However, with the rake at a different location, for instance where the maximum single-rake analysis mode power level was 117.4 dB, the mode power level estimate would have been 1.4 dB higher than the transmitted power level of 116.0 dB. With the flange exit condition, the potential for error in estimating transmitted mode power levels with one rake gets larger.

Table 1
Propagating mode power levels in decibels (Re: 10^{-12}) comparing single-rake and dual-rake analyses of the in-duct measured data with either the lip or flange exit conditions. 480 Hz, mode $(2, 0)$.

Exit Type	$+x$	$-x$	Movable	Fixed	Transmit.	$\Delta^{(*)}$
Lip	116.1	99.6	115.7–117.4	116.3	116.0	0.3
Flange	116.4	106.0	114.1–118.6	118.1	116.0	2.1

$^{(*)}$ Fixed rake power level - Transmitted power level

III. Numerical Calculations

The NASA Glenn Broadband Aeroacoustic Stator Simulation (BASS) code was used to perform numerical calculations to simulate the acoustic field generated by a source at one end of a duct open at the other end allowing sound to radiate outward. The computed results from when the exit of the duct was open with either a thin or infinite-flange exit condition were used to test the accuracy of the computations by comparing the reflection matrix results determined from the computed data with results from analytical theory. The code was then used to simulate the acoustic field inside the experimental duct facility.

III.A. Numerical Solution of the Governing Equations

The BASS code is an unsteady computational aeroacoustics code that uses explicit fourth-order time marching schemes combined with high-order spatial differencing schemes to accurately solve the unsteady nonlinear Euler or Navier-Stokes equations.[14,17–21] Using a finite-difference time-domain approach, the BASS code solves these equations in chain-rule, curvilinear form. For topological flexibility, the code uses structured multiblock grids. BASS is written in standard Fortran 2008 for portability and maintainability and is parallelized using the MPI-2 standard.[22] BASS has been tested on a range of compilers and MPI implementations, and has been validated on a number of benchmark aeroacoustics problems.[18,20,23]

The BASS code has a number of spatial differencing schemes, artificial dissipation methods, and explicit time marching schemes implemented. For this work, the BASS code was run using the HALE-RK67 time marching scheme[24] to solve the three-dimensional, unsteady, non-linear, Euler equations with no mean flow present. An automatic shock-capturing dissipation model[25] was used, based on the explicit filters of Kennedy and Carpenter.[26] The Tam and Webb 7-point optimized fourth-order dispersion-relation-preserving (DRP) scheme was used for the spatial differencing.[27]

III.B. Computational Details

The computational domain had a far-field boundary outside the duct, continued into the duct and had another boundary at the acoustic driver location inside the duct. The incoming acoustic modes were imposed at this latter boundary. The Giles[28] nonreflecting boundary condition was used to allow outgoing waves to exit the computational domain with minimal reflection. At the driver location, this boundary condition was combined with the source term imposing the acoustic modes.

A reference grid was generated using the GridPro/az3000 grid generator.[29] This reference grid had a duct wall of zero thickness and is known as a thin duct. The duct wall was made thicker by removing grid blocks from the reference grid. A thicker walled duct was chosen with a wall thickness of $0.28R$, where $R = 0.61\,\mathrm{m}$ (24 inches) is the duct radius. This duct is known as the 'medium'-flanged duct and the dimensions coincide with the dimensions of the experimental duct facility previously discussed. All grid blocks were then removed outside the duct to the outer computational boundary effectively simulating a third duct with an open end with an infinite, solid flange attached. In all cases, the duct length for the numerical calculations was 2.54 m (100 inches). The grids had a minimum of 10 grid points per wavelength of the highest-frequency acoustic modes, which was well within the resolution capabilities of the DRP scheme. The grid was clustered radially and axially in the region of the duct exit as shown in Fig. 5 of an expanded view of the grid near the exit edge of the duct.

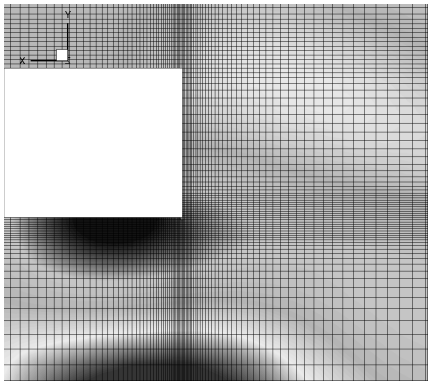

Fig. 5. Near outer surface grid for a circular duct with a finite flange at the open end. Pressure contours are shown on the surface for propagating (2,2) mode.

III.C. Open End Duct Results

The acoustic field was computed for the sound propagating toward the open end for both the thin and the infinite-flange open-end duct geometries. The source was a single acoustic mode imposed on the cross-sectional plane at the driver boundary with a frequency of 960 Hz. The shape of the mode for the acoustic pressure was given by Eq. (B.6) with an amplitude $|P^+_{m\mu}| = 1.4186$ Pa for the desired (m, μ) mode. (1.4186 Pa is equivalent to a nondimensional pressure of 10^{-5} at standard day conditions for the speed of sound c and the air density ρ.) The acoustic velocities at the source were determined from the solution to the momentum equations.

The post-processing of the numerically generated acoustic field in the duct was performed using the fixed microphone analysis described in Appendix A with 31 radial locations each with 64 azimuthal points and produced the mode coefficients for the modes propagating in each direction within the duct. A single propagating mode was generated by the source. As the mode interacts with the open end, energy was reflected back into the duct with the same mode shape. To balance the energy at the open end where some energy was reflected back into the duct and the remainder radiated outward from the open end, some energy was converted into other modes of the same circumferential order. If these modes are not cut off, they will propagate away from the open end and back toward the source. The equation that governs the acoustic pressure under these circumstances is of the form[12,30]

$$p(x, r, \theta, t) = P^+_{m\mu}\left[E^+_{m\mu}(r)e^{jk^+_{m\mu}x}e^{jm\theta} + \sum_{\nu=0}^{\infty} R_{m\mu\nu}E^-_{m\nu}(r)e^{jk^-_{m\nu}x}e^{jm\theta}\right]e^{-j\omega t} \tag{8}$$

where $R_{m\mu\nu}$ is the complex reflection coefficient matrix in which each term has a magnitude and a phase $\Psi_{m\mu\nu}$, $|R_{m\mu\nu}|\exp(j\Psi_{m\mu\nu})$. If $\mu = \nu$, $R_{m\mu\mu}$ is the reflection coefficient for the (m, μ) incident mode. For $\mu \neq \nu$, $R_{m\mu\nu}$ represents the conversion coefficients of the incident (m, μ) mode into (m, ν) modes propagating or decaying in the opposite direction. (This paper uses the term conversion as given in Cho.[31] The term scatter is commonly used.) The numerical data from multiple axial locations were post-processed to obtain the $+x$- and $-x$-direction mode coefficients. The coefficients of reflection and conversion were computed by dividing the $-x$-direction propagating complex mode coefficients by the coefficient of the single $+x$-direction propagating mode. These results were compared to results from theoretical calculations.[12,30] Fig. 6 shows the magnitude and phase of reflection and conversion coefficients determined from the computed data compared with the results computed from theory for each of the three indicated single incident modes $(2, 0)$, $(2, 1)$, and $(2, 2)$. These three modes propagate in the duct. All other modes are cut off and decay rapidly if generated.

Table 2
Identification for grid clustering near the open end of the duct.

Name	$\Delta r/R$	$\Delta x/R$
coarse	0.0145	0.0417
fine	0.00428	0.002253

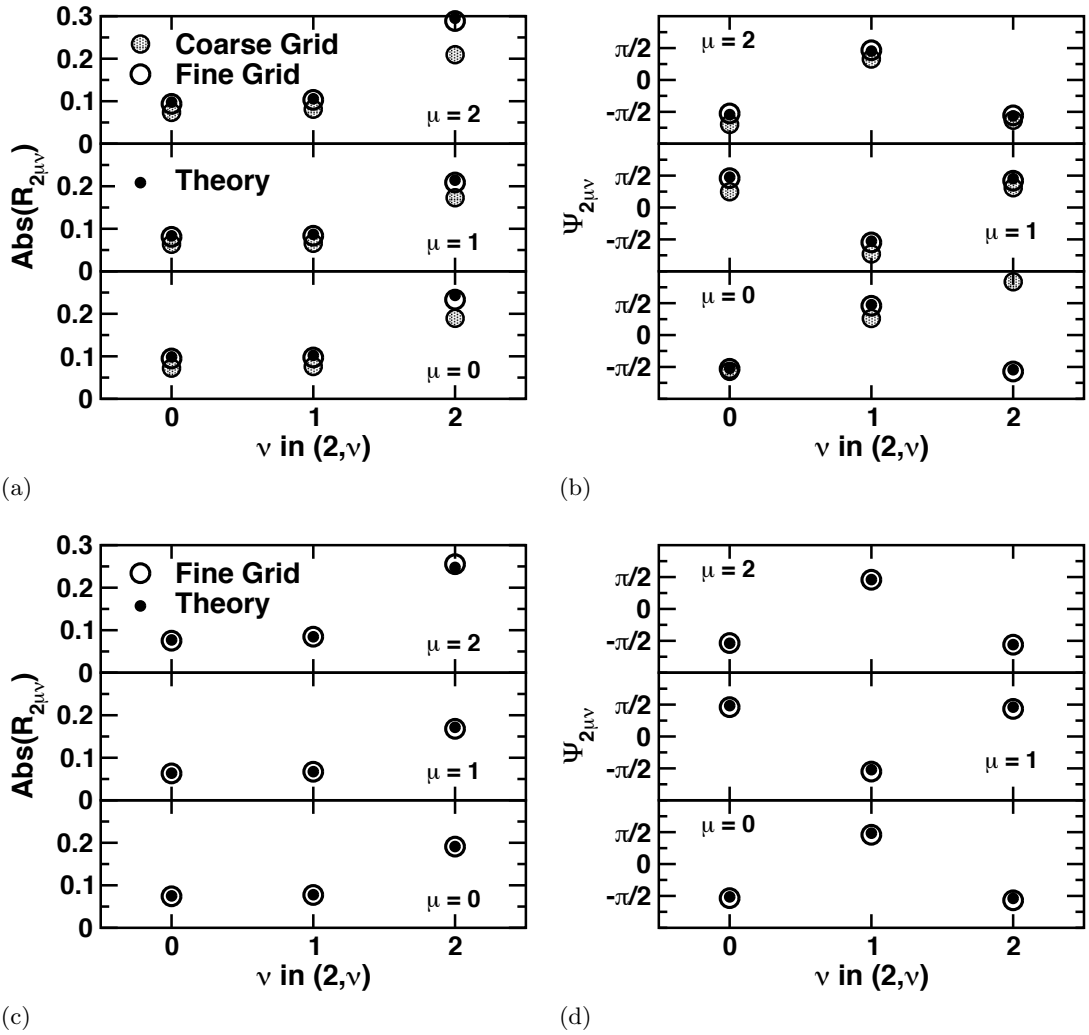

Fig. 6. Duct reflection and conversion coefficients for the single $(2, \mu)$ incident mode returning as $(2, \nu)$ modes. Solid black symbols are theory results. Shaded circle symbols are results from BASS calculations with 'coarse' grid. Open circle symbols are results from BASS calculations with 'fine' grid. 960 Hz. (a) Reflection matrix magnitude – Thin duct. (b) Reflection matrix phase – Thin duct. (c) Reflection matrix magnitude – Infinite flange. (d) Reflection matrix phase – Infinite flange.

The BASS calculations were first performed using a 'coarse' grid defined by the grid clustering near the exit given in Table 2. Figs. 6a and 6b show the computed magnitudes and phases, respectively, of the reflection and conversion coefficients from the numerical data for the thin duct compared to the results computed from the theory by Rienstra.[30] The relatively large deviations in the 'coarse'-grid results compared to theory were due to insufficient spatial grid resolution at the open end to properly handle the energy transfer among the interacting modes. The sharp corner where the duct wall ends creates a grid singularity resulting in first-order accuracy in the numerical solution.[32] The effect of increased clustering to the 'fine' grid, given in Table 2, shows the BASS computed data much closer to the theoretical results in both magnitude and phase. The results show that it was easier to resolve the $(2,0)$ and $(2,1)$ modes upon reflection or conversion from any incident mode. These modes have less radial variation than the $(2,2)$ mode. The open end singularity causes more difficulty in accurately computing the $(2,2)$ mode at the point of reflection or conversion from any incident mode. The reflection and conversion coefficients determined from the BASS computed data were accurate compared to theory within 4.4% for the magnitude and within 7.5% for the phase using the 'fine' grid.

Similar results are shown in Figs. 6c and 6d for the infinite-flange, open duct condition. Here, the reflection and conversion coefficients from the Zorumski[12] theory are given for comparison to the numerical results using the 'fine' grid. In general, it was less difficult and more accurate to compute the solution near the infinite-flange duct open end compared with the computations for the thin duct results at the same grid resolution. The errors were all less than about 3.0% for the magnitude and 6.1% for the phase.

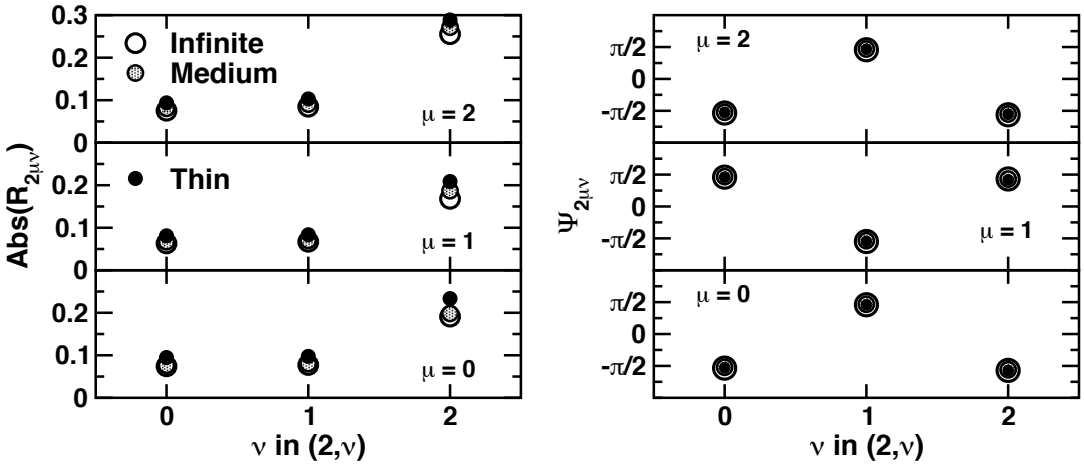

(a) (b)

Fig. 7. Duct reflection and conversion coefficients for the single $(2,\mu)$ incident mode returning as $(2,\nu)$ modes. Comparison of results from BASS calculations for the infinite-flanged duct, the 'medium'-flanged duct, and the thin duct. 960 Hz. (a) Reflection matrix magnitude – Comparison. (b) Reflection matrix phase – Comparison.

Lastly, Fig. 7 shows reflection and conversion coefficients from BASS computed data using the three single incident modes for the three open end configurations: the thin duct, the infinite-flange duct, and the 'medium'-flange duct representing the geometry of the experimental duct facility. There is no theoretical result for the reflection coefficient when non-plane-wave modes are incident upon the open end of the 'medium'-flange duct. The results in Fig. 7 show the reflection coefficient magnitudes for the 'medium'-flange duct occur near or between those for the infinite-flange duct and the thin duct. There are only small differences in phase in the reflection matrix values between the three duct exit conditions.

IV. Mode Measurement Results

The experimental results shown in Section II.C illustrated using the dual-rake measurement and data analysis method to obtain the incident and reflected mode coefficient amplitudes for a single incident mode. Those results were presented without reference to the phase of the complex coefficients. To further validate the method, comparisons are next made of the complex reflection coefficient computed from the dual-rotating rake measured data. When only a single mode may propagate, the reflection coefficient is computed from the ratio of the reflected mode coefficient to the incident mode coefficient. The geometry of the open end duct determined the physical behavior of the acoustic reflection back into the duct and thus the reflection coefficient is the same regardless of the amplitude and phase of the incident mode coefficient. This allows the results of multiple measurements to be averaged to reduce uncertainty and to allow comparisons between reflection coefficients from measured data in the experimental duct facility, from BASS computed data, and from previous measured data by others under similar modal propagation and duct termination conditions.

The simplicity of comparing reflection coefficients when the acoustic conditions in the duct allowed only one propagating mode was not found to exist when the experiment was conducted with multiple propagating modes. Under these conditions, the dual-rake measurements were used to obtain the complex mode coefficients for the $+x$- and $-x$-direction propagating modes. However, these mode coefficient results were insufficient to compute reflection matrix coefficients due to multi-modal interactions as noted below. Instead, $-x$-direction propagating mode coefficients were computed using the measured $+x$-direction propagating mode coefficients multiplied by the BASS code computed reflection matrix coefficients and these predicted mode coefficients were compared to the measured values.

IV.A. One Mode

The reflection coefficients for the open end of the duct were computed from measurements using the configuration, shown in Fig. 2, with the two rakes near the exit of the duct. The source was used to generate either a single $(2,0)$ acoustic mode at 480 Hz or a single $(6,0)$ acoustic mode at 960 Hz. Multiple rake separation measurements were made within the limits specified by Eq. (A.26) allowing multiple measurements of the same exit conditions for each mode.

Computed reflection coefficients based on results from measured data in the experimental facility with the flange exit condition are compared to predicted thin duct and infinite-flanged duct reflection coefficients in Table 3. The infinite-flange duct theory reflection coefficient magnitudes are less than the thin duct theory reflection coefficient magnitudes for both the (2.0) and $(6,0)$ modes, though the phases for both modes are nearly equal. These two cases provide reference reflection coefficient solutions. The reflection and conversion coefficients computed from the BASS generated data were shown in Fig. 6 to converge to the reference values with grid refinement and the reflection coefficients computed from BASS generated data also agreed with the Table 3 reference reflection coefficient values for the single incident mode with the single reflected mode. The duct facility in this experiment has a finite width flange for which there is no complete analytic theory for arbitrary incident modes, only for an incident plane wave.[33] Thus, the measured reflection coefficients are first checked against the plane-wave result and then compared to the converged BASS results. The plane-wave results, shown in Ando,[33] indicated that the magnitude of the reflection coefficient increases from the thin duct case as the exit flange or duct wall thickness increases over a small range of thicknesses, a range that includes the $0.28R$ flange thickness in this study. At the same time, the phase becomes more negative, that is, the phase moves clock-wise in the lower half of the complex plane. The measurement results for both the $(2,0)$ and the $(6,0)$ modes in the flanged duct, shown in Table 3, follow this trend computed for the

plane wave in both magnitude and phase compared to the thin duct results for the same modes. However, the converged BASS reflection coefficient results are lower in magnitude than both the measurement and the thin duct results and do not follow the trend from the plane-wave theory. Figure 7 shows that the converged, 'fine'-grid results for non-plane waves from the BASS 'medium'-flange computations for the reflection matrix tend to be in the vicinity of the thin duct and infinite-flange duct results for the frequencies used in this study and Table 3 confirms this for the BASS-computed single incident mode reflection coefficient. The measured reflection coefficient magnitudes are both higher than the BASS results, 38% higher at 960 Hz and 74% higher at 480 Hz.

Table 3
Comparison of open end duct reflection coefficient magnitudes and phases computed from analytical predictions, measurements, and numerical calculations.

Magnitude $\lvert R_{m\mu\mu}\rvert$							
f (Hz)	(m,μ)	$\omega R/c$	ξ	Thin Duct [a]	∞ Flange [b]	Measurement	BASS
480	$(2,0)$	5.32	1.74	0.240	0.185	0.293 ± 0.022 [c]	0.168 ± 0.001 [d]
1912	$(2,0)$	5.29	1.74	0.244		0.17 [e]	
960	$(6,0)$	10.65	1.42	0.192	0.151	0.229 ± 0.045 [c]	0.166 ± 0.001 [d]
Phase $\Psi_{m\mu\mu}$							
480	$(2,0)$	5.32	1.74	-1.356	-1.358	-1.643 ± 0.097 [c]	-1.428 ± 0.001 [d]
1912	$(2,0)$	5.29	1.74	-1.360		1.97 [e]	
960	$(6,0)$	10.65	1.42	-1.345	-1.351	-1.895 ± 0.185 [c]	-1.332 ± 0.003 [d]

[a] Rienstra[30] theory, 480 Hz and 960 Hz at 75 F, 1912 Hz standard day.

[b] Zorumski[12] theory, 75 F.

[c] Measured data, flange thickness $0.28R$, 75 F.

[d] BASS results correspond to measured data.

[e] Ville & Silcox[34] measured data, stated as 'unflanged' duct, standard day.

The differences between measured reflection coefficients and predictions can be high. Ville & Silcox[34] show differences from 25% to 100% between measured and predicted reflection coefficients using modes (2,0), (4,0), and (6,0) in a thin, finite-wall-thickness duct considered to be sufficiently close to an 'unflanged' duct. Typically the magnitude of their measured reflection coefficients were much higher than their given theoretical values especially towards the mode cut-off frequency. As frequency increased, the discrepancies in the reflection coefficient magnitude became smaller, but phase discrepancies remained large. Their measurements were made with microphones mounted in the duct wall at multiple axial locations. An example of their results is shown in Table 3 for the $(2,0)$ mode at the same normalized frequency and cutoff ratio (See Appendix C) as in the current measured data. The magnitude of the reflection coefficient is shown to be 30% lower than the theoretical, thin-duct value and the phase difference is large. Akoum & Ville[35] found similar levels of differences for measurements in a finite-flanged duct compared to the infinite-flange predictions of Zorumski.[12] They used a two-microphone method with the axially separated pair traversed around inside of the duct.

The single incident mode measurements were repeated with the lip exit mounted to the end of the experimental duct facility. The inner surface of the lip angles away from the duct axis at about 60 degrees. Table 4 shows the measured reflection coefficient magnitudes and phases for the incident $(2,0)$ and $(6,0)$

modes. These magnitudes are less than those for the flange exit condition shown in Table 3, as expected from the results shown in Fig. 4. The measured reflection coefficients are compared to reflection coefficients computed from BASS data and to a measured reflection coefficient magnitude from Ville & Silcox[34] for a $(2,0)$ mode where a 57-deg. bellmouth was mounted at the duct exit. This value was also less than their 'unflanged' duct reflection coefficient magnitude (Table 3). They also present a theoretical result based on the theory by Cho[31] for a hyperboloid-shaped inlet. The hyperboloid surface curves away from the duct axis and extends to infinity along a line making an angle of opening that intersects the duct axis at $x = 0$. The results estimated from plots in Ville & Silcox[34] for the 57-deg. hyperboloid opening are shown in Table 4 along with the results from BASS computations confirming these estimated reflection coefficient magnitudes and phases. The reflection coefficient magnitude for the $(2,0)$ mode in the hyperboloid terminated duct is 35% larger than that from the Ville & Silcox measurement, but when compared to the 60-deg. lip results, the hyperboloid results are much lower. The BASS results for the lip exit condition are similar in magnitude to the hyperboloid results but with a large difference in phase. As can be seen, the reflection coefficient magnitudes for the measured data are larger than those for the BASS results. The trends followed by the measured reflection coefficients for the lip exit are lower magnitudes and larger negative phase values compared to the flange exit condition in agreement with the trends computed from the BASS data.

Table 4
Comparison of open end duct with inlet attachment reflection coefficient magnitudes and phases computed from analytical predictions, measurements, and numerical calculations.

Magnitude $\lvert R_{m\mu\mu}\rvert$						
f (Hz)	(m,μ)	$\omega R/c$	ξ	Hyperboloid [a]	Measurement	BASS
480	$(2,0)$	5.32	1.74		0.152 ± 0.011 [b]	0.053 ± 0.001 [c]
960	$(6,0)$	10.65	1.42		0.107 ± 0.022 [b]	0.040 ± 0.001 [c]
1912	$(2,0)$	5.29	1.74	0.057	0.037 [d]	0.052 ± 0.001 [e]
	$(6,0)$	10.0		0.039		0.044 ± 0.001 [e]
Phase $\Psi_{m\mu\mu}$						
480	$(2,0)$	5.32	1.74		-2.297 ± 0.197 [b]	-3.043 ± 0.009 [c]
960	$(6,0)$	10.65	1.42		-2.194 ± 0.401 [b]	-2.824 ± 0.038 [c]
1912	$(2,0)$	5.29	1.74	-0.420		-0.419 ± 0.001 [e]
	$(6,0)$	10.0		-0.210		-0.290 ± 0.010 [e]

[a] Cho[31] theory results estimated from plots in Ville & Silcox,[34] standard day.

[b] Measured data, lip with 60 deg entry angle, 75 F.

[c] BASS results correspond to measured data.

[d] Ville & Silcox[34] data, bellmouth with 57 deg entry angle.

[e] BASS input parameters set to match $\omega R/c$, standard day, hyperboloid exit.

IV.B. Multiple Modes

Dual-rake measurements were taken in the experimental duct facility with the flange exit condition at the end of the duct. The CFANS source was set to generate $m = 2$ circumferential modes at a source frequency of 960 Hz. Under these conditions, as in the simulated data study and in the BASS computations, three propagating modes could be excited within the duct. During measurements, the absolute phasing of the

sources was not controlled and, unlike the computations where only one propagating mode was generated by the source, all three of the possible propagating modes were generated. Each of these three modes were individually incident upon the open end creating modes propagating back toward the source through reflection and conversion. The resulting modes propagating toward the source were a combination of all the modes generated by each of the three incident modes. According to Eq. (8), one propagating mode incident upon the exit generates all propagating modes in the opposite direction through reflection and conversion. When all incident propagating modes are included, the equation for the acoustic pressure field has the form of Eq. (C.1) where all $-x$-direction propagating modes have coefficients determined from a combination of incident mode coefficients given as

$$P^-_{m\nu} = \sum_{\mu=0}^{N^+_{\max}-1} P^+_{m\mu} R_{m\mu\nu} \qquad \nu = 0, 1, 2, \ldots . \tag{9}$$

Thus, the analysis of the dual-rake measurement data with three incident modes present in the duct produced the complex mode coefficients $P^+_{2\mu}$ and $P^-_{2\nu}$ $(\mu, \nu = 0, 1, 2)$. These values are insufficient to determine the complex reflection matrix coefficients since Eq. (9) gives a total of three complex equations for $P^-_{2\nu}$ (ignoring any damped mode contribution) containing nine complex unknowns $R_{2\mu\nu}$. To validate the measurements that provide the complex $P^-_{2\nu}$ mode coefficients for the three incident modes, the reflection matrix values were determined from the BASS simulations.

The data from dual-rake measurements was analyzed for different rake separation distances using the same locations shown in Fig. 4 with the reference rake at $x_2/R = -0.083$. The movable rake was limited to locations between $x_1/R = -0.158$ to $x_1/R = -0.323$ as defined by Eq. (A.26) for the combination of the $(2, 0)$, $(2, 1)$, and $(2, 2)$ propagating modes. From the data-processing analysis, the values obtained for the complex mode coefficients $P^+_{2\mu}$ and $P^-_{2\nu}$ were found to have approximately the same amplitude when the movable rake was at $x_1/R = -0.229$, -0.271, and -0.312. However, the phase appeared to be random; a result from not controlling the absolute phase at the source. Regardless of the separation distance, once the source system was set and the measurements completed, the $+x$-direction propagating mode coefficients should have the same relative amplitudes and phases. The ratios of the $+x$-direction propagating complex mode coefficients P^+_{21}/P^+_{20}, P^+_{22}/P^+_{20}, and P^+_{22}/P^+_{21} were computed for the data measured at the above three x_1/R locations and found to be near constant in magnitude and phase. Using the ratios for the $x_1/R = -0.229$ location as a reference and normalizing the ratios from the locations at $x_1/R = -0.271$ and -0.312, the average normalized magnitude and phase for all ratios were 0.98 ± 0.025 and -0.027 ± 0.038 (-3.7 to $+0.6$ deg), respectively, compared to the ideal normalized magnitude of 1.0 and phase 0 deg. This shows that the $+x$-direction mode coefficients were consistently measured with the correct relative amplitudes and phases. The average amplitude of these mode coefficients was $|P^+_{2\mu}| = \{4.45, 7.14, 16.05\}$ Pa $(\mu = 0, 1, 2)$. These modes generate the combined $-x$-direction modes that had average amplitudes $|P^-_{2\nu}| = \{1.65, 3.01, 5.35\}$ Pa $(\nu = 0, 1, 2)$.

By computing the ratios of $-x$-direction mode coefficients to the $+x$-direction mode coefficients, the relative mode coefficient magnitudes and phases remain about constant from one measurement to the next measurement allowing averages to be computed. Fig. 8 compares the average magnitudes and phases of the complex mode coefficient ratios determined from measured and computed data. The computed results used Eq. (9) to obtain $P^-_{2\nu}$ where the $P^+_{2\mu}$ mode coefficients came from the measured data and the reflection matrix values $R_{2\mu\nu}$ were from the BASS computed data results shown in Fig. 7 for the 'medium'-flange duct simulating the duct facility. The trends are the same in both magnitude and phase between the two sets of results. The percent error difference in the magnitude is 13% at $\nu = 2$, 17% at $\nu = 0$, and 34% at

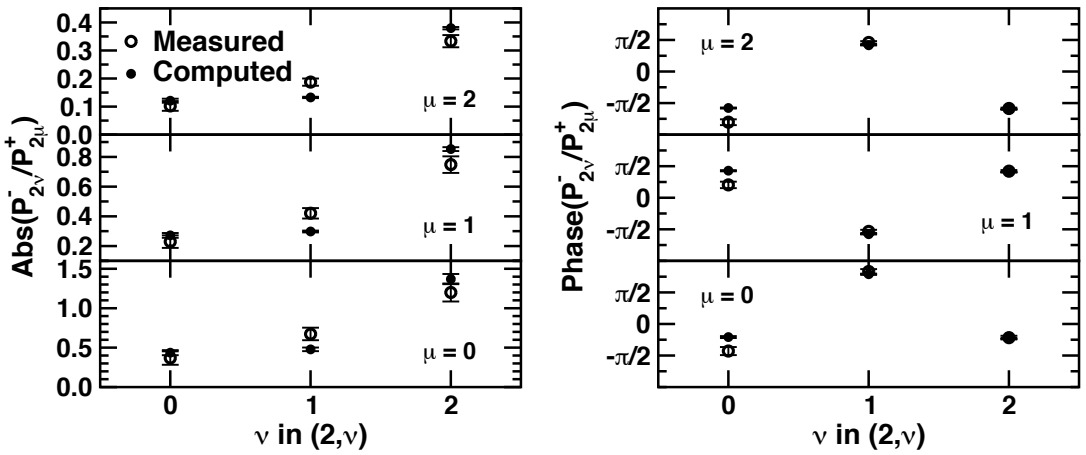

(a) (b)

Fig. 8. Ratios of $-x$-direction mode coefficients to $+x$-direction mode coefficients for three incident modes in an open end duct with flanged geometry, 960 Hz. Comparing ratios based on measured data with computed data. Symbols are averages with one standard deviation uncertainty. (a) Mode coefficient ratio magnitude. (b) Mode coefficient ratio phase.

$\nu = 1$. For the phase, the error difference is large at $\nu = 0$ (between 32% and 70%) but is much smaller at $\nu = 1$ and 2 (between 2% and 10%). These results show that the analysis of the dual-rake measured data in the experimental duct facility has extracted appropriate values for the complex $+x$- and $-x$-direction mode coefficients when multiple propagating modes are present and interacting with the open duct termination.

V. Concluding Remarks

The rotating rake mode measurement data analysis process[1,2,5,6] has been extended from the analysis of data from a single rotating rake to include the data simultaneously collected from an axially-offset, co-rotating second rake. Since measurements at a single axial rake location will not provide sufficient data to determine the direction of propagating modes, a second rake measurement, axially separated from the first, is minimally necessary. The analysis of the data from each rake is initially the same, providing circumferential mode coefficients at each microphone location identified with the harmonic number of the blade-passing frequency and the circumferential mode number. As the modes propagate within the duct, the amplitudes and phases change. By taking measurements from two rotating microphone rakes simultaneously, these changes are captured in the circumferential mode coefficients. The two sets of circumferential mode coefficients are considered to be the sum of radial basis functions some of which may be viewed as propagating in one direction and some propagating in the other direction. The remainder modes are evanescent and may have some amplitude at one measurement location but have little or no amplitude at the other location in the direction that damping occurs. With a rearrangement of the equations for a least-squares fit of the radial basis functions to the circumferential mode coefficients (as shown in A.4.), evanescent modes are properly included in the fit to obtain the mode coefficients that apply to modes propagating in both directions.

Experiments were conducted to validate the dual-rake measurement and data analysis system. Initially, a single propagating mode was generated and measurements were made within the duct for two different duct terminating geometries. The analysis of the measured data confirmed that the amplitude of the incident mode coefficient was about the same level for the two different geometries and the reflected mode amplitude changed as expected. Also, the analysis of the single-rake measurements showed that the mode amplitude followed

the amplitude of the standing wave within the duct. For validation, ratios of reflected mode coefficients to incident mode coefficients from measured data were compared to those from computed data. For the latter, analytical computations would be preferred but the experimental duct geometry was not amenable to an analytical approach. Therefore, numerical calculations were used to simulate acoustic propagation within the experimental duct facility.

The results from the numerical data generated by the NASA Glenn Broadband Aeroacoustic Stator Simulation (BASS) code were shown to agree with the analytical results for the thin duct, the infinite-flange duct, and the hyperboloid-exit duct. Thus, the reflection coefficients and other mode coefficient ratios computed from the BASS data generated from the duct simulation were compared to those values computed from the rotating rake measured data. When one mode was propagating in the duct, the magnitude of the reflection coefficients from the measured data were higher than those from the BASS computed data. This difference is large yet it is comparable to the differences between measured and theoretical results found using other different measurement methods. Consistent results were found between measured and computed reflection coefficients when the geometry was changed. In both cases, changing from the flange exit to the flow-lip exit resulted in a decrease in the magnitude of the reflection coefficient and a larger negative phase shift. The results were complicated when three modes were propagating in the duct since the $+x$-direction modes interacted at the exit to generate the $-x$-direction modes. In this case, the reference $-x$-direction mode coefficients were generated using the measured $+x$-direction mode coefficients multiplied by reflection and conversion coefficients computed from BASS simulation data. The same trends were followed between computed and measured mode coefficient ratio magnitudes and phases with generally smaller errors in phase than in magnitude.

Appendix A. Review of Mode Measurement Data Analysis

The sound fields of interest are those generated by rotating machinery inside of ducted systems. As described by Sofrin in Groeneweg et al.,[36] this field contains information about the acoustic source mechanisms that, if properly analyzed, will help reveal how the sound is generated and will provide a guide toward mitigating the sound. In most cases of interest, the sound generated inside these systems is at frequencies where the wavelengths are less than the physical dimensions of the duct allowing the sound to bounce around creating patterns of sound in the cross-sectional area of the duct called modes. Information about these modes is a desired result from acoustic measurements that may be made in a fixed frame of reference to the duct or in a rotating frame of reference.

The physical measurement of acoustic modes in a duct using fixed microphones has been conducted with a low number of microphones moved to multiple locations,[37] with a larger number of microphones usually arranged in a fixed array along the duct wall,[36] or with a large number of microphones mounted on incrementally traversed rakes,[38] flush-mounted in wall arrays,[39] or a combination of both.[40] Optimizing these mounting arrangements have been studied for various test conditions.[41] The analysis of the measured data using temporal and spatial Fourier transforms to obtain the complex mode coefficients was discussed by Moore[37] and by Sofrin.[36] This analysis is reviewed below as a prelude to the rotating frame analysis. A large array of microphones placed within a duct is impractical when flow is present since fixed probes create wakes that cause the creation of spurious noise. However, this is not an issue for numerically generated data. A time signal may be extracted from any point in the computational field. The data generated by the numerical calculations simulating the duct acoustic problems in this paper were analyzed using the fixed-frame data analysis.

The rotating frame analysis is performed on the measured data from a relatively small number of mi-

crophones mounted on a rotating rake in a duct where flow is often present. This approach reduces the complexity of a large number of microphones or the time consumption of incrementally traversing a set of microphones and, hence, reducing cost.[1–3] As with the fixed-frame data analysis, the goal of analyzing rotating rake data is to obtain the complex mode coefficients for each of the measured modes. When data from one axial location or one rotating rake is analyzed, the modal coefficients are a result of the superposition of modes propagating in both directions within the duct. The coefficients of the measured modes that propagate in both directions in the duct are separately obtained when data from two axial locations or two rotating rakes axially separated are analyzed.

A.1. Fixed Microphone Analysis

For the purpose of this analysis, the acoustic field in the duct is generated by a numerical calculation. As the calculation progresses in time, each spatial grid point in the field provides a time history of the acoustic field at that point. These data can then be sampled at particular points in the field and further processed to determine the acoustic modes in the duct including mode coefficient and direction of propagation.

The unsteady solution or time history was desired at particular locations on cross-sectional planes perpendicular to the axis in the acoustic field within the circular duct. At specific axial locations, radial points were chosen on the planar surface and at each radius, there was a set of uniformly-spaced, azimuthal points. Bilinear interpolation, as necessary, was applied to the data to obtain a time history at the desired locations.

The acoustic field in the duct may be represented analytically as a combination of acoustic modes

$$p(x,r,\theta,t) = \mathrm{Re}\left\{\sum_s \sum_{m=-M}^{M} C_m^s(x,r) e^{jm\theta} e^{-j2\pi f_s t}\right\} \tag{A.1}$$

where p is the real acoustic pressure that is shown to be a cyclical function of time t and the azimuthal direction θ since in a circular duct, the pressure must be repetitive in that direction. It is also shown to be a general summation of spatial modes $C_m^s(x,r)$ over all source frequencies f_s and circumferential mode indices m where the index ranges over a finite number of modes denoted by the general value M. To begin the process of extracting the modal information, transforms must be performed on the discretized time history. For numerically generated data, the time histories are generated at discrete time steps $t_i = i\Delta t$, $i = 0, 1, 2, \ldots, I-1$, where I is the total number of samples in the time history. A source frequency f_s is related to the frequency resolution $f_s = s\Delta f$ where $\Delta f^{-1} = I\Delta t$ and the variable s is, in general, not necessarily an integer. The discrete time history form of Eq. (A.1) for the acoustic pressure at a particular spatial location (x_1, r_1, θ_1) becomes

$$p(x_1,r_1,\theta_1,i) = \mathrm{Re}\left\{\sum_s \sum_{m=-M}^{M} C_m^s(x_1,r_1) e^{jm\theta_1} e^{-j2\pi si/I}\right\}. \tag{A.2}$$

Performing the discrete Fourier transform

$$\hat{P}(\ell) = \frac{1}{I}\sum_{i=0}^{I-1} p(i) e^{j2\pi\ell i/I} \qquad \ell = 0, 1, 2, \ldots, I-1 \tag{A.3}$$

on Eq. (A.2) results in an equation of the form

$$\hat{P}(x_1,r_1,\theta_1,\ell) = \sum_s \left[\frac{1}{2}\sum_{m=-M}^{M} C_m^s(x_1,r_1) e^{jm\theta_1} h(s-\ell) + \frac{1}{2}\sum_{m=-M}^{M} C_m^{s*}(x_1,r_1) e^{-jm\theta_1} h(I-s-\ell)\right] \tag{A.4}$$

where h is the function

$$h(s-\ell) = \frac{1}{I}\exp\left[-j\pi(s-\ell)\left(\frac{I-1}{I}\right)\right]\frac{\sin[\pi(s-\ell)]}{\sin[\pi(s-\ell)/I]} \tag{A.5}$$

that accounts for spectral leakage if s is not an integer. The second term on the right side of Eq. (A.4) is the complex conjugate of the first term. For s to be an integer at f_s, then $s = f_s/\Delta f = f_s I\Delta t = f_s I/\widetilde{f}$ requires $f_s I$ to be an integer multiple of the sampling rate $\widetilde{f}$ or the rate of the time step Δt. The result is that at $\ell = s$, an integer, $h \to \delta$ a unit delta function.

Only the frequency terms at $\ell = s$ in Eq. (A.4) are of interest. A spatial discrete Fourier transform is now performed on N_θ points in the azimuthal direction at a fixed radial location r_1 and at a fixed axial location x_1. In Eq. (A.4), θ_1 is replaced by $\theta_{\hat{\nu}} = 2\pi\hat{\nu}/N_\theta$, $\hat{\nu} = 0, 1, 2, \ldots, N_\theta - 1$, and upon using the discrete transform

$$\mathcal{P}(\hat{\mu}) = \frac{1}{N_\theta}\sum_{\hat{\nu}=0}^{N_\theta-1}\hat{P}(\hat{\nu})e^{-j2\pi\hat{\mu}\hat{\nu}/N_\theta} \qquad \hat{\mu} = 0, 1, 2, \ldots, N_\theta - 1 \tag{A.6}$$

we can get an equation of the form

$$\mathcal{P}(x_1, r_1, \hat{\mu}, s) = \frac{1}{2}\sum_{m=0}^{M} C_m^s(x_1, r_1)\delta(m-\hat{\mu}) + \frac{1}{2}\sum_{m=M}^{1} C_{-m}^s(x_1, r_1)\delta(N_\theta - m - \hat{\mu}). \tag{A.7}$$

The outputs of this spatial transform are the complex acoustic pressure amplitudes for the circumferential mode at the specified radial and axial location. For circumferential modes that exist in the duct with $m \geq 0$, their complex coefficients will appear in the first term on the right side at $\hat{\mu} = m$. The coefficient values for any circumferential mode with $m < 0$ will appear in the second term at $\hat{\mu} = N_\theta - m$. (Note that a positive integer m is used in this term.) To avoid overlap of the left and right terms of Eq. (A.7), we require that $M - \hat{\mu} < N_\theta - M - \hat{\mu}$ or $N_\theta > 2M$. Thus, the number of samples in θ must be more than twice the highest circumferential mode number of interest. With conditions satisfied, the complex circumferential mode coefficients are extracted from the transformed data

$$C_m^s(x_1, r_1) = 2\mathcal{P}(x_1, r_1, m, s). \tag{A.8}$$

A.2. Rotating Microphone Analysis

For a microphone in a rotating frame, the measured data are analyzed to obtain the circumferential mode coefficient at each radial measurement location. Consider the signal

$$p(x, \theta, r, t) = \mathrm{Re}\left\{\sum_s \sum_{m=-M}^{M} C_m^s(x, r)e^{jm\theta}e^{-j2\pi sB\Omega t}\right\} \tag{A.9}$$

where the source frequency f_s in Eq. (A.1) is replaced by $sB\Omega$ since the sound is generated by a rotating fan with Ω, the shaft speed in revolutions per second, B, the number of blades, and, s, the harmonic number $s = 1, 2, \ldots$. The signal is sampled synchronously with the shaft speed and ensemble averaged over a period $T = I\Delta t$. This reduces the uncorrelated broadband noise in favor of the tonal content of the signal. As previous, the circumferential mode index m ranges over a finite number of modes denoted by the general value M.

A microphone generating a signal that is described by Eq. (A.9) is located at a fixed axial location x_1, a fixed radial location r_1, and at an azimuthal location $\theta = \theta_1 + \phi$ where ϕ is an azimuthal offset from

some reference. The microphone rotates according to $\theta_1 = 2\pi\Gamma t$ where Γ is the rotational speed of the rake. Eq. (A.9) becomes

$$\begin{aligned} p(x_1,\phi,r_1,t) &= \mathrm{Re}\left\{\sum_s \sum_{m=-M}^{M} C_m^s(x_1,r_1) e^{jm\theta} e^{-j2\pi sB\Omega t}\right\} \\ &= \mathrm{Re}\left\{\sum_s \sum_{m=-M}^{M} C_m^s(x_1,r_1) e^{jm(\theta_1+\phi)} e^{-j2\pi sB\Omega t}\right\} \\ &= \mathrm{Re}\left\{\sum_s \sum_{m=-M}^{M} C_m^s(x_1,r_1) e^{jm\phi} e^{-j2\pi(sB\Omega - m\Gamma)t}\right\}. \end{aligned} \tag{A.10}$$

This equation shows that the source blade passage frequency harmonic $sB\Omega$ has been Doppler shifted to $f_n = sB\Omega - m\Gamma$. For analysis, the signal must be digitized. Choosing a sampling frequency $\widetilde{f} = 1/\Delta t$ and defining $f_n = n\Delta f$, where $\Delta f^{-1} = I\Delta t$, the argument of the last exponential term in Eq. (A.10) becomes $2\pi(sB\Omega - m\Gamma)t = 2\pi ni/I$. Taking the discrete Fourier transform (Eq. (A.3)) of the microphone signal, we obtain for any spectral component of the signal:

$$\hat{P}_m^s(x_1,\phi,r_1,\ell) = \frac{1}{2} C_m^s(x_1,r_1) e^{jm\phi} h(n-\ell) + \frac{1}{2} C_m^{s*}(x_1,r_1) e^{-jm\phi} h(I-n-\ell). \tag{A.11}$$

For rotating machinery, sampling is done at integer multiples of the shaft rotation, $\widetilde{f} = \Omega\widetilde{n}$, where $\widetilde{n}$ is the number of samples per shaft revolution. Given that the total number of samples in the digitized time history I is related to the time and frequency resolutions, $I = 1/(\Delta t \Delta f)$, the discrete frequency index n is defined by

$$n = \frac{1}{\Delta f}(sB\Omega - m\Gamma) = \frac{I}{\Omega\widetilde{n}}(sB\Omega - m\Gamma) \tag{A.12}$$

The total number of samples in the time history may be represented by

$$I\left(\frac{\text{samples}}{\text{history}}\right) = \widetilde{n}\left(\frac{\text{samples}}{\text{shaft rev.}}\right) \times \widetilde{n}_r\left(\frac{\text{shaft rev.}}{\text{history}}\right) \tag{A.13}$$

or

$$I\left(\frac{\text{samples}}{\text{history}}\right) = \widetilde{n}\left(\frac{\text{samples}}{\text{shaft rev.}}\right) \times \frac{\Omega}{\Gamma}\left(\frac{\text{shaft rev.}}{\text{rake rev.}}\right) \times n_r\left(\frac{\text{rake rev.}}{\text{history}}\right) \tag{A.14}$$

where we note that

$$\widetilde{n}_r = \frac{\Omega}{\Gamma} n_r. \tag{A.15}$$

Using Eqs. (A.13) to (A.15), Eq. (A.12) becomes

$$n = \widetilde{n}_r sB - m n_r. \tag{A.16}$$

In order to eliminate spectral leakage, n must be an integer. Eq. (A.16) indicates that the spectrum contains families of spikes about each harmonic s having the complex mode coefficients of the $\pm m$ circumferential modes. These coefficients can be simply extracted using

$$C_m^s(x_1,r_1) = 2\hat{P}_m^s(x_1,\phi,r_1,\ell) e^{-jm\phi} \tag{A.17}$$

where $\ell = n$ for the desired harmonic number s and circumferential mode number m.

To illustrate, assume n is an integer. For a fixed rake ($\Gamma = 0, n_r = 0$), the spectrum given by Eq. A.11

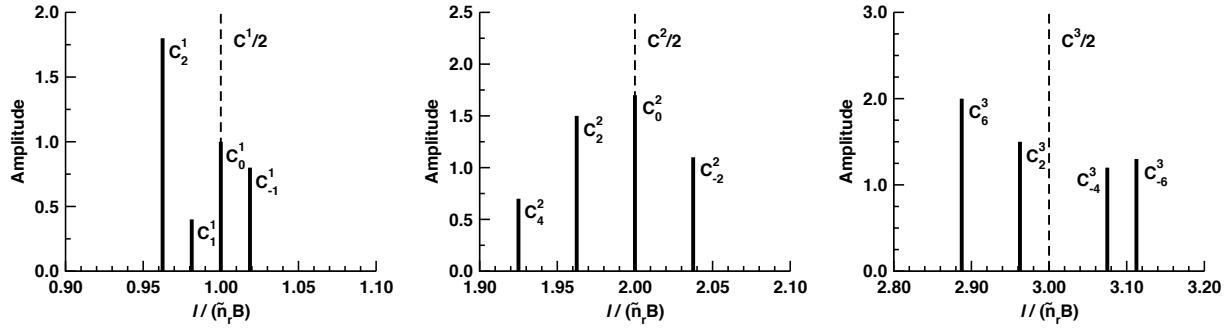

(a) (b) (c)

Fig. A.1. Illustration of the separation of circumferential mode amplitudes from data measured by a rotating rake in a duct. Dashed lines are the amplitudes of the blade passage frequency harmonics measured by a stationary rake. Solid lines are the separated circumferential mode amplitudes from rotating rake measurements, Table A.1. Normalized index $\ell/(\widetilde{n}_r B) = s - (m/B)(\Gamma/\Omega)$. (a) First harmonic. (b) Second harmonic. (c) Third harmonic.

will contain spikes at $\ell = n = \widetilde{n}_r sB$ for each harmonic of the blade passage frequency with an amplitude that is the sum of all m propagating modes at that harmonic frequency. After applying a fixed rotation speed Γ, the spikes at the $\widetilde{n}_r sB$ harmonics separate into a family of spikes at n defined by Eq. (A.16) with mode coefficients C_m^s. This is shown in Fig. A.1 for the real-valued, circumferential mode coefficient amplitudes given in Table A.1. The faster the rake rotates (Γ increases), the wider the separation there is between the spikes. For $m < 0$, the mode amplitude spikes move to frequencies higher than the blade passage frequency harmonic and for $m > 0$, the mode amplitude spikes move to lower frequencies.

To determine criterion on the rake revolution speed Γ, we consider the cases of rotor-alone generated modes and rotor-stator interaction modes. A rotor alone with B blades generates circumferential modes up to $m = \pm sB$ where s is the blade passage frequency harmonic number.[42] To keep the mode families about the harmonics separated, the lowest index ℓ^- with $m > 0$ at the next harmonic, $s+1$, must be greater than the highest index ℓ^+ with $m < 0$ at harmonic s.

$$\ell^- > \ell^+$$

$$n_r\left((s+1)B\frac{\Omega}{\Gamma} - (s+1)B\right) > n_r\left(sB\frac{\Omega}{\Gamma} + sB\right)$$

$$\frac{\Omega}{\Gamma} > 1 + 2s \tag{A.18}$$

Rotor-stator-interaction-generated circumferential modes are determined by $m = sB - k_v V$, where V is the number of stator vanes and $k_v = 0, \pm 1, \pm 2, \ldots$.[42] Again, to keep mode families separated $\ell^- > \ell^+$ or

$$n_r\left((s+1)B\frac{\Omega}{\Gamma} - (s+1)B - |k_v|\,V\right) > n_r\left(sB\frac{\Omega}{\Gamma} + sB + |k_v|\,V\right)$$

$$\frac{\Omega}{\Gamma} > 1 + \frac{2}{B}\left(sB + |k_v|\,V\right) = 1 + \frac{2}{B}|m| \tag{A.19}$$

Both Eq. (A.18) and Eq. (A.19) show that $\Omega > \Gamma$, that is, the rotating measurement rake revolves at a speed slower than the fan shaft speed. In practice, Ω/Γ has ranged from 100 to 250. If $B = 20$, then $|m|$ of $O(10^3)$ can easily be accommodated.

The discrete Fourier transform may be used with any integer value of I to transform a signal given by

Table A.1
Circumferential mode coefficient amplitudes.

s	m		s	m		s	m	
1	0	$C_0^1 = 1.0$	2	0	$C_0^2 = 1.7$	3	2	$C_2^3 = 1.5$
	1	$C_1^1 = 0.4$		2	$C_2^2 = 1.5$		6	$C_6^3 = 2.0$
	2	$C_2^1 = 1.8$		4	$C_4^2 = 0.7$		-4	$C_{-4}^3 = 1.2$
	-1	$C_{-1}^1 = 0.8$		-2	$C_{-2}^2 = 1.1$		-6	$C_{-6}^3 = 1.3$
Total		$C^1 = 4.0$			$C^2 = 5.0$			$C^3 = 6.0$

Eq. (A.10). To use the more efficient finite Fourier transform algorithm, I must be an integer power of 2. This limits the choices in either Eq. (A.13) or Eq. (A.14). The number of samples per shaft revolution can easily be an integer power of 2. The remaining factors are limited by the choice of Ω/Γ. Table A.2 gives example parameter values where Ω/Γ is within the range of practical values given above.

Table A.2
Example parameter definitions for analyzing rotating rake microphone signals using the finite Fourier transform.

$\widetilde{n}$	Ω/Γ	n_r	$\widetilde{n}_r$	I
2^7 (128)	2^7 (128)	2^2 (4)	2^9	2^{16}
2^7 (128)	2^8 (256)	2^2 (4)	2^{10}	2^{17}

A.3. Single Axial Location or Single Rotating Rake Analysis

The analysis of the microphone signal, either in a fixed or rotating frame, has provided the complex circumferential mode coefficient $C_m^s(x_1, r_1)$ at the location of the microphone. At a single axial location these values are functions of the radial mode content in the duct following

$$C_m^s(x_1, r_\alpha) = \sum_{\mu=0}^{N_{\max}-1} P_{sm\mu} E_{sm\mu}(r_\alpha; x_1) \qquad \alpha = 1, 2, \ldots, N_1 \tag{A.20}$$

where the circumferential mode coefficients have been collected from different radii at a fixed axial location. Eq. (A.20) represents the attempt to further decompose the measured circumferential mode data into an approximate series of weighted radial basis functions $E_{sm\mu}(r_\alpha; x_1)$. For a rotating measurement system mounted in a duct, microphones are mounted at N_1 different radii on a rake that rotates within the duct. If there is one rake with all the microphones measuring at a single axial location, then they each produce one value of $C_m^s(x_1, r_\alpha)$ at their respective r_α location. With the radial basis functions (described in Appendix B) previously computed at a frequency with harmonic number s and for the duct conditions at the rake axial location x_1, Eq. (A.20) is solved for the complex radial mode coefficients, $P_{sm\mu}$, using the least-squares method. The solution is to minimize the residual sum of squares

$$e = \|\mathbf{c} - \mathbf{BP}\|_2^2 \tag{A.21}$$

where

$$\mathbf{c} = \begin{bmatrix} C_m^s(x_1, r_1) & \dots & C_m^s(x_1, r_{N_1}) \end{bmatrix}^{\mathrm{T}}$$

is a vector comprised of the measured complex circumferential mode data of length $n_p = N_1$,

$$\mathbf{B} = \begin{bmatrix} E_{sm0}(r_1; x_1) & \dots & E_{sm(N_{\max}-1)}(r_1; x_1) \\ \vdots & \dots & \vdots \\ E_{sm0}(r_{N_1}; x_1) & \dots & E_{sm(N_{\max}-1)}(r_{N_1}; x_1) \end{bmatrix}$$

is a matrix of complex coefficients from the radial basis functions of size $n_p \times n_c$, $n_c = N_{\max}$, and

$$\mathbf{P} = \begin{bmatrix} P_{sm0} & \dots & P_{sm(N_{\max}-1)} \end{bmatrix}^{\mathrm{T}}$$

is the complex solution vector for the radial mode coefficients of length n_c. By ensuring that the number of measurement points N_1 is greater than the number of radial basis functions $N_{\max}$, the problem is overdetermined, $n_p > n_c$, and a solution to this linear problem is easily computed using the singular value decomposition method. This method provides the best approximation to solving the linear least-squares problem for over-determined systems and it is robust, handling problems where $\mathbf{B}$ is close to being singular. (See Lawson & Hanson[16] for details.)

A.4. Dual Axial Location or Dual Rotating Rake Analysis

It has been assumed in solving Eq. (A.20) for the mode coefficients $P_{sm\mu}$, using $N_{\max}$ radial basis functions, that the modes propagate in only one direction. The form of the solution for the acoustic pressure is

$$p(x, \theta, r, t) = P_{m\mu} E_{m\mu}(r) e^{-j(\omega t - m\theta - k_{m\mu} x)} \tag{A.22}$$

where $E_{m\mu}$ is a general function of r that forms the basis function for the least-squares fit, ω is the radian frequency, and $k_{m\mu}$ is the axial wave number for the specified m, the circumferential mode number, and μ, the radial mode number. Using the convention that the x-axis is positive in the direction away from the source, Eq. (A.22) indicates that a positive real axial wave number is required for the mode to propagate away from the sound source within the duct. The sound in the duct, in general, does not just propagate in one direction. The duct will be finite in length and reflections will occur sending sound back toward the source. Thus, modes may propagate in both the $+x$ direction and the $-x$ direction. Following Åbom,[43] Akoum & Ville,[35] and Schultz et al.,[44] the $P_{m\mu}$ term may be written as a function of the axial location x using the exponential term in Eq. (A.22),

$$P_{m\mu}(x) = P_{m\mu}^{+} e^{jk_{m\mu}x} + P_{m\mu}^{-} e^{-jk_{m\mu}x} \tag{A.23}$$

where $P_{m\mu}^{+}$ and $P_{m\mu}^{-}$ are the coefficients for the modes propagating in the $+x$ direction and the $-x$ direction, respectively, and the basis function is the same in both directions. To determine these mode coefficients, data must be collected at a second axial location. Taking data at two axial locations, x_1 and x_2, (Rademaker[45] and Akoum & Ville[35]) results in a system of equations

$$\begin{aligned} P_{m\mu}(x_1) &= P_{m\mu}^{+} e^{jk_{m\mu}x_1} + P_{m\mu}^{-} e^{-jk_{m\mu}x_1} \\ P_{m\mu}(x_2) &= P_{m\mu}^{+} e^{jk_{m\mu}x_2} + P_{m\mu}^{-} e^{-jk_{m\mu}x_2} \end{aligned} \tag{A.24}$$

that can be solved for $P^+_{m\mu}$ and $P^-_{m\mu}$.

The approach, so far, has assumed constant conditions in the duct and that all modes to be included in a least-squares fit are propagating. Depending on the axial location where the data are obtained, it may be appropriate to include information related to evanescent modes that could cause problems. Using Eq. (A.24) for an extreme example, the wave number k could represent an evanescent or a damped mode decaying in the $+x$ direction going from x_1 to x_2. The mode could be sufficiently damped by reaching x_2 that the exponential function would be zero. This results in coefficients multiplying $P^+_{m\mu}$ and $P^-_{m\mu}$ containing zeroes. For the general least-squares problem, this leads to a singular matrix when computing the normal equation for the fit. Modifications, shown next, are required to avoid this problem.[46]

The mode coefficients for the $+x$- and $-x$-direction propagating modes are now determined in the rotating frame by including the data measured by a second rake, offset axially and co-rotating with the first rake. The signals from the second rake microphones are acquired simultaneously with those from the first and Fourier analyzed to obtain the complex circumferential mode coefficients. The signals at each rake location are the sums of $+x$-direction and $-x$-direction propagating and perhaps evanescent modes. However, it may be appropriate to consider the presence of evanescent modes in one direction and not the other. For example, measurements taken near the duct exit may be expected to include evanescent modes from reflections back from the exit but none toward the exit if the source is far enough away. Thus, the total number of $+x$-direction modes, $N^+_{\max}$, included in the fit may differ from the total number of $-x$-direction modes, $N^-_{\max}$. To extract the radial mode coefficients, the measured circumferential mode coefficients are written as the sum of radial basis functions as follows:

$$\begin{aligned}
C^s_m(x_1, r_\alpha) &= \sum_{\mu=0}^{N^+_{\max}-1} \left\{ P^+_{sm\mu} e^{jk^+_1 x_1} \right\} E^+_{sm\mu}(r_\alpha; x_1) \\
&+ \sum_{\mu=0}^{N^-_{\max}-1} \left\{ P^-_{sm\mu} e^{jk^-_2 x_2} \right\} E^-_{sm\mu}(r_\alpha; x_1) e^{j(k^-_1 x_1 - k^-_2 x_2)} \\
C^s_m(x_2, r'_{\alpha'}) e^{-jm\phi} &= \sum_{\mu=0}^{N^+_{\max}-1} \left\{ P^+_{sm\mu} e^{jk^+_1 x_1} \right\} E^+_{sm\mu}(r'_{\alpha'}; x_2) e^{j(k^+_2 x_2 - k^+_1 x_1)} \\
&+ \sum_{\mu=0}^{N^-_{\max}-1} \left\{ P^-_{sm\mu} e^{jk^-_2 x_2} \right\} E^-_{sm\mu}(r'_{\alpha'}; x_2) \qquad \text{(A.25)} \\
&\qquad \alpha = 1, 2, \ldots, N_1 \qquad \alpha' = 1, 2, \ldots, N_2
\end{aligned}$$

where ϕ is the azimuthal offset between the rake at x_1 and the rake at x_2. The axial wave numbers depend on the frequency through the harmonic number s and the mode numbers m and μ and the subscripts '1' and '2' apply for the solution of the eigenvalue problem at the rake locations x_1 and x_2. Also, r_α and $r'_{\alpha'}$ denote that radial locations of microphones on the two rakes may differ in location and number. This formulation:

- Rescales the coefficients and radial basis functions to properly handle evanescent modes.
- Acknowledges the axial eigenvalues and the radial basis functions in the upstream propagating direction are different from those in the downstream propagating direction when non-uniform mean flow is present. Also, unlike Eq. (A.24), the axial eigenvalues in Eq. (A.25), k^+ and k^-, contain the appropriate signs for propagation and/or decay in the indicated direction.
- Allows for small changes in flow and duct area with axial distance. Thus we make the following

approximation for a slowly varying axial wave number[46]

$$\int_{x_1}^{x_2} k \, \mathrm{d}x \approx k_2 x_2 - k_1 x_1$$

for $|k_2 - k_1|$ much less than both $|k_2|$ and $|k_1|$.

The form of Eq. (A.25) indicates that the measured data from both rakes were identically analyzed as if $\phi = 0$ in Eq. (A.17). For the least-squares fit, the rake at x_1 was chosen as the reference and the azimuthal offset ϕ was then added to the rake data from location x_2.

To solve Eq. (A.25) for the complex radial mode coefficients, we again use the least-squares method. The solution is to minimize the residual sum of squares, Eq. (A.21), where in the dual-rake analysis

$$\mathbf{c} = \begin{bmatrix} C_m^s(x_1, r_1) & \dots & C_m^s(x_1, r_{N_1}) & C_m^s(x_2, r'_1)e^{-jm\phi} & \dots & C_m^s(x_2, r'_{N_2})e^{-jm\phi} \end{bmatrix}^{\mathrm{T}}$$

is a vector of length $n_p = N_1 + N_2$ comprised of the measured complex circumferential mode data,

$$\mathbf{B} = \begin{bmatrix} E_{sm0}^+(r_1; x_1) & \dots & E_{sm0}^-(r_1; x_1)e^{j(k_1^- x_1 - k_2^- x_2)} & \dots \\ \vdots & \dots & \vdots & \dots \\ E_{sm0}^+(r_{N_1}; x_1) & \dots & E_{sm0}^-(r_{N_1}; x_1)e^{j(k_1^- x_1 - k_2^- x_2)} & \dots \\ E_{sm0}^+(r'_1; x_2)e^{j(k_2^+ x_2 - k_1^+ x_1)} & \dots & E_{sm0}^-(r'_1; x_2) & \dots \\ \vdots & \dots & \vdots & \dots \\ E_{sm0}^+(r'_{N_2}; x_2)e^{j(k_2^+ x_2 - k_1^+ x_1)} & \dots & E_{sm0}^-(r'_{N_2}; x_2) & \dots \end{bmatrix}$$

is a matrix of size $n_p \times n_c$, $n_c = N_{\max}^+ + N_{\max}^-$, containing complex coefficients derived from the radial basis functions, and

$$\mathbf{P} = \begin{bmatrix} \left\{P_{sm0}^+ e^{jk_1^+ x_1}\right\} & \left\{P_{sm1}^+ e^{jk_1^+ x_1}\right\} & \dots & \left\{P_{sm0}^- e^{jk_2^- x_2}\right\} & \left\{P_{sm1}^- e^{jk_2^- x_2}\right\} & \dots \end{bmatrix}^{\mathrm{T}}$$

is the solution vector of length n_c for the complex radial mode coefficients at the current rake locations x_1 and x_2. The complex radial mode coefficients $P_{sm\mu}^+$ and $P_{sm\mu}^-$ that apply at $x = 0$ are obtained from the solution vector by translating back the distance x_1 and x_2, respectively, as indicated to $x = 0$. By ensuring that the total number of measurement points n_p is greater than n_c, the problem is overdetermined and a solution to this linear problem is again easily computed using the singular value decomposition method.

Duct conditions and axial rake locations that would produce a singularity or near singularity in the inverse matrix calculation using $\mathbf{B}$ in Eq. (A.21) are to be avoided. Using previous work on errors in two-microphone, in-duct measurements, Åbom[43] provides practical limits that for the no-flow case are given by

$$0.1\pi < k_{m\mu} \, |x_2 - x_1| < 0.8\pi. \tag{A.26}$$

These limits are followed in the in-duct, two-microphone, higher-order mode measurements in Akoum & Ville[35] and are, also, followed in this paper.

Appendix B. Radial Basis Functions

The goal of the analysis of single- or dual-axial location or rotating rake data is to obtain the coefficients of the measured modes that propagate in one or both directions within the duct. For that to occur, we must determine the radial basis functions that are required to solve either Eq. (A.20) or Eq. (A.25) for the complex mode coefficients.

The acoustic pressure p in an annular or circular duct with a non-uniform mean flow is governed by a third order equation derived from combining the linearized momentum and energy equations, assuming the static pressure is constant.[47]

$$\frac{\mathrm{D}^3 p}{\mathrm{D}t^3} + c^2 \left[2 \frac{\partial (c\mathrm{M})}{\partial r} \frac{\partial^2 p}{\partial x \, \partial r} - \frac{1}{c^2} \frac{\partial c^2}{\partial r} \frac{\mathrm{D}}{\mathrm{D}t} \frac{\partial p}{\partial r} - \frac{\mathrm{D}}{\mathrm{D}t} \nabla^2 p \right] = 0 \tag{B.1}$$

where

$$\frac{\mathrm{D}}{\mathrm{D}t} = \frac{\partial}{\partial t} + c\mathrm{M} \frac{\partial}{\partial x}$$

and ∇^2 is the Laplace operator in cylindrical coordinates. This equation accounts for the compressibility of the flow and allows both the Mach number M and the speed of sound c to be functions of the radial direction.

For the computational and experimental results presented in this paper, the duct is circular with radius R and the walls are hard. Hence the boundary condition at the wall, $r = R$, given in terms of the acoustic pressure, is

$$\frac{\partial p}{\partial r} = 0 \tag{B.2}$$

and the boundary condition at the duct centerline, $r = 0$, is given by

$$\begin{aligned} \frac{\partial p}{\partial r} &= 0 \qquad m = 0 \\ p &= 0 \qquad m \neq 0. \end{aligned} \tag{B.3}$$

The complete numerical solution of Eq. (B.1) is found in Dahl & Sutliff.[6]

The results in this paper have no flow present. Hence, the analysis of the more general Eq. (B.1), using the separation of variables solution in the form given by Eq. (A.22), reduces to

$$\frac{\partial^2 E}{\partial r^2} + \frac{1}{r} \frac{\partial E}{\partial r} - \frac{m^2}{r^2} E + \kappa^2 E = 0 \tag{B.4}$$

where κ^2 is given by

$$\kappa^2 = \left(\frac{\omega}{c} \right)^2 - k^2. \tag{B.5}$$

The solution for the basis function is given in closed form

$$E_{m\mu}(r) = \sqrt{\mathcal{N}_{m\mu}^2} \mathrm{J}_m(\kappa_{m\mu} r) \tag{B.6}$$

where J_m is a cylindrical Bessel function of the first kind and the factor

$$\mathcal{N}_{m\mu}^2 = \left[\left(1 - \frac{m^2}{\kappa_{m\mu}^2 R^2} \right) \mathrm{J}_m(\kappa_{m\mu} R)^2 \right]^{-1}$$

is used to normalize the Bessel function J_m and ensures that the integral of E^2 across the area of the duct equals the duct cross-sectional area. The argument of the Bessel function, $\kappa_{m\mu} R$, represents the μ^{th} zero of

the derivative of the Bessel function J'_m, that is $J'_m(\kappa_{m\mu}R) = 0$ where $m = 0, 1, 2, \ldots$, and $\mu = 0, 1, 2, \ldots$. The solution for constant conditions has determined a radial eigenvalue. The required axial eigenvalue to determine mode propagation or decay is obtained from the solution to Eq. (B.5).

Appendix C. Testing Method with Simulated Data

Simulated data was used to test the analysis technique to separate the direction of modes propagating in a duct. The simulated data was constructed from a set of modes in a circular duct propagating at a single frequency. Following Eq. (6), we used

$$C_m(x,r) = \sum_{\mu=0}^{N_{\max}^+-1} P_{m\mu}^+ E_{m\mu}^+(r) e^{jk_{m\mu}x} + \sum_{\nu=0}^{N_{\max}^--1} P_{m\nu}^- E_{m\nu}^-(r) e^{-jk_{m\nu}x} \tag{C.1}$$

to obtain the circumferential mode coefficients where the radial basis functions are given by Eq. (B.6) for the conditions of a constant area, circular duct with no mean flow.

Eq. (C.1) was used to compute the complex circumferential mode coefficients that represent the results of simulated rotating rakes with seven radial measurement locations in a duct with three propagating modes. Setting $m = 2$, the circumferential mode coefficients were computed using the parameter values shown in Table C.1. The magnitudes of the axial eigenvalues are the same in both directions. The three lower order

Table C.1
Eigenvalues, mode amplitudes (Pa), and cutoff ratios for a simulation with 3 propagating modes in both directions and 1 damped mode in the $-x$ direction. 960 Hz, $m = 2$.

μ	$k_{2\mu}R$	$\kappa_{2\mu}R$	$\lvert P_{2\mu}^+\rvert$	$\lvert P_{2\mu}^-\rvert$	$\xi_{2\mu}$
0	10.368	3.054	1.204	0.036	3.539
1	8.477	6.706	1.118	0.224	1.612
2	4.175	9.969	1.266	1.241	1.084
3	$j7.526$	13.170	0.000	$0.1^{(*)}$	0.821

$^{(*)}$ at reference location $x/R = -0.083$

radial modes are propagating in both directions with cutoff ratios $\xi_{m\mu} = \omega/\kappa_{m\mu}c$ greater than 1 and there is one cutoff mode decaying in the $-x$ direction with a reference amplitude of 0.1 at $x/R = -0.083$. Fig. C.1 shows the computed mode coefficient amplitudes from the single-rake analysis of the data as a function of the axial location. These results are compared to the standing-wave amplitudes computed by

$$A_{m\mu}(x) = \left| P_{m\mu}^+ e^{jk_{m\mu}x} + P_{m\mu}^- e^{-jk_{m\mu}x} \right| \tag{C.2}$$

where the reflecting point is at $x = 0$. The standing wave amplitude $A_{m\mu}$ is at a maximum value at $x = 0$ and decreases for $x < 0$ until a minimum is reached, then increases again and so forth up the duct. A single measurement rake placed at the maximum of the standing wave ($x = 0$) will provide the data that when analyzed according to the single rake procedure will return the amplitude of the standing wave. As shown in Fig. C.1, as the rake is moved in the $-x$ direction, over a total of 21 locations, the data provided to the single-rake analysis reproduced the local standing wave amplitude. The comparison of the computed mode amplitudes with the standing wave amplitudes is identical. The analysis also obtains the correct damped mode amplitude. Obviously, the assumption for single-rake operation that modes only propagate in one

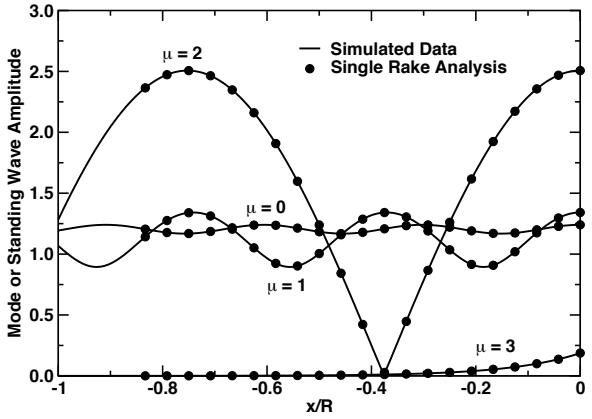

Fig. C.1. Comparison of single-rake analysis for mode amplitude to the standing wave amplitude for 3 propagating waves in both directions and 1 damped mode. 960 Hz, $m = 2$.

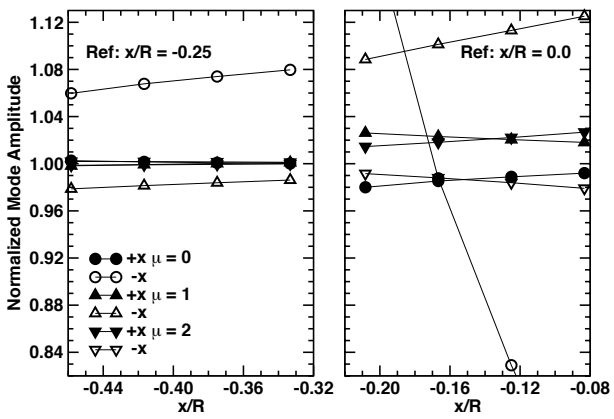

Fig. C.2. Mode amplitudes from dual-rake analysis of simulated data using only 3 propagating modes in both directions in the fit process. Normalized by Table C.1 amplitudes. 960 Hz, $m = 2$.

direction ($+x$ in this case) requires significantly reduced mode amplitudes in the other direction. The $\mu = 0$ mode has a $-x$-direction mode with an amplitude two orders of magnitude smaller than the $+x$-direction mode amplitude and still shows a small oscillation about the $|P_{20}^{+}| = 1.204$ Pa value.

The dual-rake analysis was next performed using the simulated data. Two sets of analyses were performed; one with the reference rake at $x = 0$ and a second set with the reference rake at $x/R = -0.25$. The movable rake was moved along the $-x$-direction locations indicated in Fig. C.2. To keep within the limitations for the rake separation given by Eq. (A.26) for all three propagating modes, the results are limited to a maximum separation of 0.24, determined for the $(2, 0)$ mode, and a minimum separation of 0.075 for the $(2, 2)$ mode. This analysis was first completed with the three propagating modes in both directions plus one damped mode in the $-x$ direction. The propagating mode amplitudes shown in Table C.1 were recovered and the proper damped mode amplitude was computed for the movable rake location. A second analysis was computed using only the three propagating modes in each direction. The least-squares fit redistributed the amplitude changes due to the presence of the damped mode to the propagating modes affecting the computed propagating mode amplitudes. The results are shown in Fig. C.2 where the propagating mode amplitudes are each normalized by the exact mode amplitudes shown in Table C.1. Where the damped mode has a large effect, the normalized mode amplitude is further from the 1.0 value. The effects are larger nearer $x = 0$ where the damped mode amplitude is larger and the effects decrease in the $-x$ direction as the damped mode amplitude decreases. The largest effects are found in the smaller amplitude $(2, 0)$ and $(2, 1)$ $-x$-direction propagating modes. The four larger amplitude propagating modes have similar levels of error. In this simulation where the two rakes are placed near $x = 0$, the largest error for not including the damped mode in the least-squares fit model is up to 3 % in the $(2, 2)$ $+x$-direction propagating mode amplitude that translates to a small 0.2 dB error in the mode power level.

The simulated data recreated the conditions in a duct with incident and reflected modes from a boundary. We showed that the single-rake measurement and data analysis resulted in mode coefficients with amplitudes that were the amplitudes of the standing wave in the duct. It was only when any reflected mode coefficient amplitude was small that the single-rake analysis provided the mode coefficient for the propagating mode in one direction. Using the dual-rake analysis, the mode coefficients were obtained for both modes propagating in the two directions. The simulation also showed that if there was significant evanescent mode amplitude at a measurement location that was not included in the fitting process, the fitting process would put erroneous

amounts of energy into the propagating modes. Thus, evanescent modes need to be properly included in the fit, when necessary, to obtain the correct mode coefficients for the propagating modes. The number of evanescent modes to include in the fit process can be determined from an analysis of the decay of the mode amplitude for any expected mode. Alternatively, it was found that the propagating mode coefficients changed little if additional evanescent modes were included in the fit process beyond the one or two, if any, significant evanescent modes.

References

[1]Cicon, D. E., Sofrin, T. G., and Matthews, D. C., "Investigation of a Continuously Traversing Microphone System for Mode Measurement," NASA CR-168040, PWA-5846-26, November 1982.

[2]Hall, D. G., Heidelberg, L., and Konno, K., "Acoustic Mode Measurements in the Inlet of a Model Turbofan Using a Continuously Rotating Rake: Data Collection/Analysis Technique," AIAA Paper No. 93-0599, 1993.

[3]Sutliff, D. L., "Rotating Rake Turbofan Duct Mode Measurement System," NASA TM-2005-213828, October 2005.

[4]Sutliff, D. L., "Rotating Rake Mode Measurements Over Passive Treatment in a Ducted Fan," NASA TM-2006-214493, December 2006.

[5]Sutliff, D. L., "Turbofan Duct Mode Measurements Using a Continuously Rotating Microphone Rake," *Int. J. of Aeroacoustics*, Vol. 6, No. 2, 2007, pp. 147–170.

[6]Dahl, M. D. and Sutliff, D. L., "Numerical Technique for Analyzing Rotating Rake Mode Measurements in a Duct With Passive Treatment and Shear Flow," AIAA Paper No. 2007-3679, 2007.

[7]Envia, E., Tweedt, D. L., Woodward, R. P., Elliott, D. M., Fite, E. B., Hughes, C. E., Podboy, G. G., and Sutliff, D. L., "Fan Noise Prediction," *Assessment of NASA's Aircraft Noise Prediction Capability*, edited by M. D. Dahl, NASA TP-2012-215653, chap. 5, 2012.

[8]Heidelberg, L. J. and Hall, D. G., "Inlet Acoustic Mode Measurement Using a Continuously Rotating Rake," *J. Aircraft*, Vol. 32, No. 4, July 1995, pp. 761–767.

[9]Cicon, D. E. and Sofrin, T. G., "Method for Extracting Forward Acoustic Wave Components from Rotating Microphone Measurements in the Inlets of Turbofan Engines," NASA CR-195457, April 1995.

[10]Meyer, H. D., "Effect of Inlet Reflections on Fan Noise Radiation," *AIAA J.*, Vol. 34, No. 9, 1996, pp. 1771–1777.

[11]Nallasamy, M., Sutliff, D. L., and Heidelberg, L. J., "Propagation of Spinning Acoustic Modes in Turbofan Exhaust Ducts," *J. Prop. Power*, Vol. 16, No. 5, September 2000, pp. 736–743.

[12]Zorumski, W. E., "Generalized Radiation Impedances and Reflection Coefficients of Circular and Annular Ducts," *J. Acoust. Soc. Am.*, Vol. 54, No. 6, 1973, pp. 1667–1673.

[13]Sutliff, D. L., "A Mode Propagation Database Suitable for Code Validation Utilizing the NASA Glenn Advanced Noise Control Fan and Artificial Sources," AIAA Paper No. 2014-0719, 2014.

[14]Hixon, R., Nallasamy, M., and Sawyer, S., "Parallization Strategy for an Explicit Computational Aeroacoustics Code," AIAA Paper No. 2002-2583, 2002.

[15]Loew, R. A., Lauer, J. T., McAllister, J., and Sutliff, D. L., "The Advanced Noise Control Fan," AIAA Paper No. 2006-3150, 2006.

[16]Lawson, C. L. and Hanson, R. J., *Solving Least Squares Problems*, Prentice-Hall, Englewood Cliffs, NJ, 1974.

[17]Nallasamy, M., Hixon, R., and Sawyer, S., "Solution of Unsteady Euler Equations: Gust-Cascade Interaction Tones," *Computers and Fluids*, Vol. 36, 2007, pp. 724–741.

[18]Hixon, R., Nallasamy, M., and Sawyer, S., "Progress Towards the Prediction of Turbomachinery Noise Using Computational Aeroacoustics," Inter-Noise IN06-119, December 2006.

[19]Hixon, R., Golubev, V. V., Mankbadi, R. R., Scott, J. R., Sawyer, S., and Nallasamy, M., "Application of a Nonlinear Computational Aeroacoustics Code to the Gust-Airfoil Problem," *AIAA J.*, Vol. 44, 2006, pp. 323–328.

[20]Hixon, R., Nallasamy, M., Sawyer, S., and Dyson, R., "Comparison of Numerical Schemes for a Realistic Computational Aeroacoustics Problem," *Int. J. of Aeroacoustics*, Vol. 3, 2004, pp. 379–397.

[21]Sawyer, S., Nallasamy, M., Hixon, R., and Dyson, R. W., "A Computational Aeroacoustic Prediction of Discrete-Frequency Rotor-Stator Interaction Noise: A Linear Theory Analysis," *Int. J. of Aeroacoustics*, Vol. 3, 2004, pp. 67–86.

[22]Snir, M., Otto, S., Huss-Lederman, S., Walker, D., and Dongarra, J., *MPI - The Complete Reference*, The MIT Press, Cambridge, Mass., 1998.

[23]Hixon, R., Sescu, A., and Sawyer, S., "Vortical Gust Boundary Condition for Realistic Rotor Wake/Stator Interaction Noise Prediction Using Computational Aeroacoustics," *J. Sound Vib.*, Vol. 330, No. 16, 2011, pp. 3801–3817.

[24]Allampalli, V., Hixon, R., Nallasamy, M., and Sawyer, S., "High-Accuracy Large-Step Explicit Runge-Kutta (HALE-RK) Schemes for Computational Aeroacoustics," *J. Comp. Physics*, Vol. 228, No. 10, 2009, pp. 3837–3850.

[25]Hixon, R., Bhate, D., Nallasamy, M., and Sawyer, S., "Shock-Capturing Dissipation Schemes for Computational Aeroacoustics," AIAA Paper No. 2006-2413, May 2006.

[26]Kennedy, C. A. and Carpenter, M. H., "Several New Numerical Methods for Compressible Shear-Layer Simulations," *Appl. Num. Math.*, Vol. 14, 1994, pp. 397–433.

[27]Tam, C. K. W. and Webb, J. C., "Dispersion-Relation-Preserving Finite Difference Schemes for Computational Acoustics," *J. Comp. Physics*, Vol. 107, No. 2, 1993, pp. 262–281.

[28]Giles, M. B., "Nonreflecting Boundary Conditions for Euler Equation Calculations," *AIAA J.*, Vol. 28, 1990, pp. 2050–2058.

[29]GridPro/az3000, Program Development Company, White Plains, NY, 1993–2010.

[30]Rienstra, S. W., "Acoustic Radiation from a Semi-Infinite Annular Duct in a Uniform Subsonic Mean Flow," *J. Sound Vib.*, Vol. 94, No. 2, 1984, pp. 267–288.

[31]Cho, Y. C., "Rigorous Solutions for Sound Radiation from Circular Ducts with Hyperbolic Horns or Infinite Plane Baffle," *J. Sound Vib.*, Vol. 69, No. 3, 1980, pp. 405–425.

[32]Hixon, R., Nallasamy, M., and Sawyer, S., "Effect of Grid Singularities on the Solution Accuracy of a CAA Code," AIAA Paper No. 2003-0879, 2003.

[33]Ando, Y., "On the Sound Radiation from Semi-Infinite Circular Pipe of Certain Wall Thickness," *Acustica*, Vol. 22, No. 4, 1969, pp. 219–225.

[34]Ville, J.-M. and Silcox, R. J., "Experimental Investigation of the Radiation of Sound From an Unflanged Duct and a Bellmouth, Including the Flow Effect," NASA TP-1697, 1980.

[35]Akoum, M. and Ville, J.-M., "Measurement of the Reflection Matrix of a Discontinuity in a Duct," *J. Acoust. Soc. Am.*, Vol. 103, 1998, pp. 2463–2468.

[36]Groeneweg, J. P., Sofrin, T. G., Rice, E. J., and Gliebe, P. R., "Turbomachinery Noise," *Aeroacoustics of Flight Vehicles: Theory and Practice Volume 1: Noise Sources*, edited by H. H. Hubbard, NASA RP-1258, chap. 3, 1991.

[37]Moore, C. J., "In-Duct Investigation of Subsonic Fan "Rotor Alone" Noise," *J. Acoust. Soc. Am.*, Vol. 51, No. 5, 1971, pp. 1471–1482.

[38]Enghardt, L., Tapken, U., Neise, W., Kennepohl, F., and Heinig, K., "Turbine Blade/Vane Interaction Noise: Acoustic Mode Analysis Using In-Duct Sensor Rakes," AIAA Paper No. 2001-2153, 2001.

[39]Enghardt, L., Tapken, U., Kornow, O., and Kennepohl, F., "Acoustic Mode Decomposition of Compressor Noise under Consideration of Radial Flow Profiles," AIAA Paper No. 2005-2833, 2005.

[40]Tapken, U., Bauers, R., Neuhaus, L., Humphreys, N., Wilson, A., Stöhr, C., and Beutke, M., "A New Modular Fan Rig Noise Test and Radial Mode Detection Capability," AIAA Paper No. 2011-2897, 2011.

[41]Tapken, U. and Enghardt, L., "Optimization of Sensor Arrays for Radial Mode Analysis in Flow Ducts," AIAA Paper No. 2006-2638, 2006.

[42]Tyler, J. M. and Sofrin, T. G., "Axial Flow Compressor Noise Studies," *SAE Transactions*, Vol. 70, 1962, pp. 309–332.

[43]Åbom, M., "Modal Decomposition in Ducts Based on Transfer Function Measurements Between Microphone Pairs," *J. Sound Vib.*, Vol. 135, No. 1, 1989, pp. 95–114.

[44]Schultz, T., Cattafesta, L. N., and Sheplak, M., "Modal Decomposition Method for Acoustic Impedance Testing in Square Ducts," *J. Acoust. Soc. Am.*, Vol. 120, No. 6, 2006, pp. 3750–3758.

[45]Rademaker, E. R., "Experimental Validation of a Lined-Duct Acoustics Model Including Flow," Tech. Rep. Paper No. 90-WA/NCA-2, ASME, Presented at the ASME Winter Annual Meeting, Dallas, TX, Nov. 1990, 1990.

[46]Ovenden, N. C. and Rienstra, S. W., "Mode-Matching Strategies in Slowly Varying Engine Ducts," *AIAA J.*, Vol. 42, No. 9, September 2004, pp. 1832–1840.

[47]Eversman, W., "Theoretical Models for Duct Acoustic Propagation and Radiation," *Aeroacoustics of Flight Vehicles: Theory and Practice Volume 1: Noise Sources*, edited by H. H. Hubbard, NASA RP-1258, chap. 13, 1991.